Marine Structures 103 (2025) 103845

Contents lists available at ScienceDirect

Marine Structures

journal homepage: www.elsevier.com/locate/marstruc

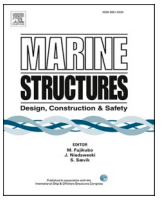

Modal matrix reduction for fully coupled integrated load analysis of floating structures

Borja Servan-Camas [a], Irene Berdugo-Parada [a,b,*], Julio Garcia-Espinosa [b], Andres Pastor-Sanchez [a,b]

[a] Centre Internacional de Mètodes Numèrics en Enginyeria (CIMNE), Gran Capitan s/n, 08034 Barcelona, Spain
[b] Escuela Técnica Superior de Ingenieros Navales (ETSIN), Technical University of Madrid (UPM), Av. de la Memoria, 28040 Madrid, Spain

ARTICLE INFO

Keywords:
Integrated load analysis
ILA
Modal matrix reduction
MMR
Hydroelasticity
Floating offshore wind turbines
Reduce order models

ABSTRACT

Structural elasticity of floating wind turbines in integrated load analysis (ILA) is typically addressed by modelling the substructure with simplified beam models. The main reason can be found in the computational cost of the structural solver when solving the fully coupled hydroelastic problems. In this work, a reduce order method based on modal matrix reduction is applied to reduce the computational cost of the structural solver. The main idea is to largely reduce the number of degrees of freedom of the structural system by retaining only those modes with significant energy.

The seakeeping hydrodynamics is solved using the finite element framework SeaFEM. The structural particulars are introduced into this framework to fully integrate the fluid-structure interaction. The hydroelastic model is also coupled with the wind turbine solver OpenFAST, resulting in a complete aero-hydro-servo-elastic tool for the ILA analysis of floating turbines.

A methodology is proposed to identify critical conditions and hotspots based on the structural energy. An application case of the present strategy is presented for a detailed structural design of the well-known OC4-DeepCwind. The consistency of the modal approximation and methodology is verified against the FE structural solution. The capabilities of the proposed ILA framework are demonstrated in a fully coupled and detailed structural analysis, instead of at component level, with a significant reduction of its computational time.

List of symbols

φ	Velocity potential
ξ	Free surface elevation
Ω	Fluid domain
$\bar{=}$	
L	Laplacian matrix
σ	Stress tensor
u	Structural displacement vector
t	Tractions vector

* Corresponding author.
E-mail address: iberdugo@cimne.upc.edu (I. Berdugo-Parada).

https://doi.org/10.1016/j.marstruc.2025.103845
Received 12 December 2024; Received in revised form 26 March 2025; Accepted 8 May 2025
Available online 17 May 2025

$\bar{\bar{M}}$	Mass matrix
$\bar{\bar{C}}$	Structural damping matrix
$\bar{\bar{K}}$	Stiffness matrix
a_i	Eigenvectors
Ω_i	Modal frequencies
q_i	Modal amplitudes
η	Critical modal damping
c_i	Rayleigh damping
E^D	Dynamic elastic energy

1. Introduction

Floating offshore wind turbine (FOWT) technology is being tested to capture the wind energy potential found in the deep-seas. Currently, the efforts to lower their levelized cost of energy (LCOE) are leading to a new generation of larger and light-weighted floating platform concepts [1]. In order to extend the lifespan of these substructures withstanding the worst sea-states that might encounter, the study of its structural behavior and fatigue damage becomes relevant. Accordingly, more research is being focused to develop higher-fidelity simulation tools for the study and cost-effective optimization of the existing structural concepts.

The simultaneous wind-waves loads acting on the substructure of FOWTs in addition to the mooring system, introduce strong aero-hydro-elastic interactions, and it is acknowledged that the elasticity of the platform has a decisive influence on the overall system dynamics [2,3]. To study these interactions, several computational tools [4–7] have been developed, being able to simulate the coupled dynamic response of FOWTs under environmental loads. These solvers allow to perform Integrated Load Analysis (ILA) where the hydrodynamic solution is typically calculated with potential flow theory, Morison's equations or a combination of both, whereas the structural one is represented with 1D beam elements. Together with a Craig-Bampton (C-B) reduction method [8,9], the structural deformations can be expressed as the superposition of natural modes. This approach is able to capture the members deformations but not local stresses, needed to predict structural failure.

If a structural analysis of the FOWT substructure is required, this is usually performed by introducing the precomputed external loads into a detailed FEM structural model based on the finite element method. This partitioned strategy implies solving the hydroelastic problem in several stages and transforming the frequency-domain hydrodynamic loads into time-domain. This approach only enables for one-way (weak) couplings which might be valid for rigid structures. When simulating flexible structures, the two-ways (strong) coupling should be considered to account for the added mass and damping induced by the water on the structure. However, it is the most common way to carry out hydroelastic analysis, due to the complexity and computational cost of solving the full three-dimensional problem in the time-domain, mostly taken by the structural solver [10].

The conventional time-domain elastic analysis of wind turbines has been generally modelled by taken into account the tower and rotor blades flexibility and considering the floater as a rigid body [11,12]. This approach is able to predict the global response of the substructure but not its local elastic response within its individual members. While this might be accurate for the analysis of small floating wind turbines, it can result in large errors on the computation of coupled natural frequencies and internal loads for larger platforms [13]. On this regard, the hydroelastic effects on the platform are starting to be studied as in [14,15] using a one-dimensional beam method and in [16,17] using a FEM solver for detailed structural analysis.

In this work, a hydroelastic solver using a structural reduced order model (ROM) based on the modal matrix reduction (MMR) [18] is tested. By retaining only those eigenmodes preserving most of the structural elastic energy, the number of structural DoF is reduced, which also results in a decrease of the structural solver computational cost. This structural model is strongly coupled with the time–domain seakeeping solver SeaFEM [19–25]. Its combination with the wind turbine solver OpenFAST [26,27], presents a coupled areo-hydro-servo-elastic numerical framework for ILA of floating wind substructure concepts. The natural structural outputs are then the modal amplitudes, allowing to compute the structural displacements, strains, and stress fields offline based on the precomputed modal amplitudes.

For many load-cases where the external loads can be assumed to be linear, the ILA framework allows to pre-compute modal response amplitude operators [MRAOs] [18]. Then, once MRAOs are known, it is straight forward to carry out dynamic realizations under irregular loads scenarios. This can largely reduce the computational times enabling its use for fatigue damage computation and operational conditions like in a digital twin. In [28], this approach was implemented on the OSI4IOT [29,30] digital platform to develop a DT for structural health monitoring.

The present hydroelastic case study procedure is applied to the semi-submersible structural design of the OC4 DeepCwind concept, named CIMNE-DeepCwind. The aim of this structural design is not to provide a reliable structural solution, but to be used as an academic benchmark case to test the capability of simulation tools for structural assessment. The structural details are presented in the appendix. A number of case studies are used to test the dynamic response of the CIMNE-DeepCwind using the proposed ILA framework.

2. Hydroelastic solver

In [10], the authors of this work developed a strategy for coupling the seakeeping hydrodynamics and structural dynamics using

solvers developed in house and integrated into the commercial packages SeaFEM [31] and RamSeries [32]. Both solvers are implemented under the same programming framework, allowing a direct communication between them and the use of OpenMP for the parallel execution of both solvers. It was reported that most of the computational time required for fully coupled analysis is taken to solve the structural dynamics. In order to overcome this bottleneck, the authors proposed a reduce order model based on modal matrix reduction [18], where the number of degrees of freedom for the structural problem can be largely reduced alongside its computational cost.

In this work, the same solvers are used, but with a different approach. First, the structural solver is used only to obtain the structural particulars such as the structural FEM matrices (mass and stiffness) or the modal base. Then, in a second stage, the seakeeping solver reads the structural particulars, building the structural dynamics equations coupled with the seakeeping hydrodynamics equations. In this way, there is no need to execute the structural solver for each hydroelastic execution.

SeaFEM also includes a mooring solver with capabilities to simulate quasistatic and dynamic FEM multi-segment lines [22,24]. The corresponding loads can then be applied to the structural solver as well.

2.1. Seakeeping model (SeaFEM)

The seakeeping model used in this work is a time-domain wave diffraction-radiation solver based on the Finite Element Method (FEM), developed in-house and integrated in the commercial package SeaFEM [31]. The mathematical and numerical models implemented in SeaFEM have been extensively verified and validated. These can be found in [10,18–25].

Using a frame of reference where the OZ axis represents the vertical direction and whose origin is located at the free surface, the governing equations are given by [20]:

$$\Delta\varphi = 0 \ in \ \Omega, \tag{1}$$

$$\partial_t\xi + (\boldsymbol{U} + \nabla_h\varphi)\cdot\nabla_h\xi - \partial_z\varphi = 0 \ on \ z = 0, \tag{2}$$

$$\partial_t\varphi + \boldsymbol{U}\cdot\nabla_h\varphi + \frac{1}{2}\nabla_h\varphi\cdot\nabla_h\varphi + g\xi = 0 \ on \ z = 0, \tag{3}$$

$$\boldsymbol{v}_\varphi\cdot\boldsymbol{n}_p \ = -\boldsymbol{v}_p\cdot\boldsymbol{n}_p \ on \ P \in \Gamma_B, \tag{4}$$

$$\begin{aligned} \boldsymbol{v}_\varphi\cdot\boldsymbol{n}_p &= 0 \ on \ P \in \Gamma_S, \\ P_p &= -\rho g(z_p + r_{pz}) - \rho\left(\frac{\partial\varphi}{\partial t} + \boldsymbol{U}\cdot\nabla\varphi + \frac{1}{2}\nabla\varphi\cdot\nabla\varphi\right), \end{aligned} \tag{5}$$

where φ is the velocity potential ($\mathbf{v}_\varphi = \nabla\varphi$), ξ is the free surface elevation, Ω is the fluid domain, $z = 0$ represents the still water level, Γ_B is the wetted surface of a floating body, Γ_S is the sea bottom surface, n_p is a normal vector to a surface at point P, v_p is the velocity of point p, z_p is the initial vertical position of point P, ∇_h is the gradient operator in the horizontal directions, and r_{pz} is the vertical displacement of P. The solution can be split into the incident and diffracted-radiated wave components:

$$\varphi = \psi + \phi \tag{6}$$

$$\xi = \zeta + \eta \tag{7}$$

where ψ and ζ are the velocity potential and wave elevation respectively for the incident wave field, and ϕ and η are the velocity potential and free surface elevation respectively for the diffracted-radiated waves respectively. The incident wave field is described by the Airy wave analytical solution. Introducing the separation of variables into the governing equations, the wave diffraction-radiation problem is obtained in terms of ϕ and η as independent variables. Details on the wave diffraction-radiation governing equations can be found in [20,21,25].

In this work the numerical solution using FEM of the above system reported in [20] will be used. It requires to solve the following system of equations:

$$\bar{\boldsymbol{L}}\phi = \boldsymbol{b}^B + \boldsymbol{b}^R + \boldsymbol{b}^{Z_0} + \boldsymbol{b}^S, \tag{8}$$

where $\bar{\mathbf{L}}$ is the Laplacian Matrix, and $\mathbf{b}^B$, $\mathbf{b}^R$, $\mathbf{b}^{Z_0}$, and $\mathbf{b}^S$ are the vectors resulting of integrating the boundary condition terms. The above system can be written clustering the nodes lying on the body surface as:

$$\begin{bmatrix} \bar{\boldsymbol{L}}_{II} & \bar{\boldsymbol{L}}_{I\Gamma_B} \\ \bar{\boldsymbol{L}}_{\Gamma_B I} & \bar{\boldsymbol{L}}_{\Gamma_B\Gamma_B} \end{bmatrix} \begin{bmatrix} \phi_I \\ \phi_{\Gamma_B} \end{bmatrix}^{n+1} = \begin{bmatrix} \boldsymbol{b}_I \\ \boldsymbol{b}_{\Gamma_B} \end{bmatrix}^{n+1} \tag{9}$$

where n refers to the nth time step, amd $\mathbf{b}_{\Gamma_B}$ contains the velocities of a point lying on the structure boundary. In the absence of forward speed, a fourth order compact Padé scheme is used to integrate the free surface boundary condition. The numerical details, as well as a

number of verification and validation cases, can be found in [20].

2.2. Structural model (RamSeries)

The structural dynamic model used in this work is based on geometrical non-linear shell finite elements. The geometrical non-linear strategy is based on the corotational method developed by Felippa and Haguen in [33]. The core element used by the corotational shell model is a 3-node element with three translations and three rotations per node, which is obtained by the combination of a membrane element and a plate element. The membrane element is based in the optimal triangle element with drilling rotation developed by Felippa in [34], while the plate element is based in the classical Discrete Kirchhoff Triangle (DKT) element first introduced in [35]. This element has shown better performance that the standard bilinear quadrilateral element generally used in marine applications [34].

The algorithm used for the time-integration is based on the approximately energy conserving scheme presented by Almeida and Awruch in [36]. The complete model has been developed in-house and integrated within the commercial package RamSeries [32]. The frame of reference used is the same as for the seakeeping model. The governing equations of the model are given by:

$$\boldsymbol{div}(\boldsymbol{\sigma}) + \boldsymbol{b} = \rho \ddot{\boldsymbol{u}} \ in \ \Omega_s, \tag{10}$$

$$\boldsymbol{u} = \overline{\boldsymbol{u}} \ on \ P \in S_u \tag{11}$$

$$\boldsymbol{\sigma} \cdot \boldsymbol{n} = \overline{\boldsymbol{t}} \ on \ P \in S_\sigma, \tag{12}$$

where $\boldsymbol{\sigma}$ is the stress tensor, $\mathbf{b}$ is a vector that includes the mass force and internal damping, Ω_s is the structural domain, $\mathbf{u}$ is the structural displacement vector field, S_u is the part of the structural external surface with prescribed displacements $\overline{\mathbf{u}}$, S_σ is the part of the structural external surface with prescribed tractions $\overline{\mathbf{t}}$. The FEM version of the above system of equations can be written as:

$$\bar{\boldsymbol{M}}\ddot{\boldsymbol{u}} + \bar{\boldsymbol{C}}\dot{\boldsymbol{u}} + \bar{\boldsymbol{K}}\boldsymbol{u} = \boldsymbol{f} \tag{13}$$

where $\bar{\mathbf{M}}$ is the mass matrix, $\bar{\mathbf{C}}$ is the structural damping matrix, $\bar{\mathbf{K}}$ is the stiffness matrix, $\boldsymbol{u}$ is the displacement vector of the structural nodes, and $\boldsymbol{f}$ is the boundary conditions vector containing the external loads and prescribed displacements. The time-discretized version of the above system of equations can be written as:

$$\bar{\boldsymbol{S}}\ \boldsymbol{u}^{n+1} = \boldsymbol{f}^{n+1} \tag{14}$$

where $\bar{\mathbf{S}}$ is the tangent stiffness matrix. The system above can be written clustering the nodes lying on the body surface as:

$$\begin{bmatrix} \bar{\boldsymbol{S}}_{II} & \bar{\boldsymbol{S}}_{I\Gamma_B} \\ \bar{\boldsymbol{S}}_{\Gamma_B I} & \bar{\boldsymbol{S}}_{\Gamma_B\Gamma_B} \end{bmatrix} \begin{bmatrix} \boldsymbol{u}_I \\ \boldsymbol{u}_{\Gamma_B} \end{bmatrix}^{n+1} = \begin{bmatrix} \boldsymbol{f}_I \\ \boldsymbol{f}_{\Gamma_B} \end{bmatrix}^{n+1} \tag{15}$$

where $\mathbf{f}_{\Gamma_B}$ contains the body boundary condition due to the fluid pressure.

2.3. Structural reduced order model

2.3.1. Modal matrix reduction

The order reduction is achieved by projecting the structural FEM solution onto a subspace of solutions with a smaller dimension [18]. In this work, this subspace is built using the MMR. Then, the structural solution can be approximated using a smaller number of degrees of freedom, being several orders of magnitudes smaller than for the structural FEM solver [37].

Splitting the static and dynamic structural loads and displacements we obtain:

$$\boldsymbol{f}(\boldsymbol{t}) = \boldsymbol{f}_D(\boldsymbol{t}) + \boldsymbol{f}_S \tag{16}$$

$$\boldsymbol{u}(t) = \boldsymbol{u}_D(t) + \boldsymbol{u}_S \tag{17}$$

where D stands for dynamic and S for static. Then, the structural equations can be also split as:

$$\bar{\boldsymbol{M}}\ddot{\boldsymbol{u}}_D(\boldsymbol{t}) + \bar{\boldsymbol{C}}\dot{\boldsymbol{u}}_D(\boldsymbol{t}) + \bar{\boldsymbol{K}}\boldsymbol{u}_D(\boldsymbol{t}) = \boldsymbol{f}_D(\boldsymbol{t}) \tag{18}$$

$$\bar{\boldsymbol{K}}\ \boldsymbol{u}_S = \boldsymbol{f}_S \tag{19}$$

where $\boldsymbol{f}_S$ represent the static loads such as self-weight, hydrostatic pressure at equilibrium position, pretension of mooring lines, … and $\boldsymbol{f}_D(t)$ represents the time dependent component of the structural loads. The dynamic component requires to solve the structural

equations many times along the simulation time. In order to reduce the computational effort required, the MMR is used. The modal basis is obtained from the free vibration problem with no damping:

$$\left(\bar{\bar{M}}^{-1}\bar{\bar{K}}\right)\boldsymbol{a} = \boldsymbol{\Omega}^2\boldsymbol{a} \tag{20}$$

Then, the structural displacements can be expressed as a linear combination of the modal displacements:

$$\boldsymbol{u_D}(\boldsymbol{t}) = \sum_{i=1}^{\boldsymbol{N_{DOF}}} \boldsymbol{q_i}(\boldsymbol{t})\boldsymbol{a_i} \tag{21}$$

Where N_{DOF} is the number of degrees of freedom of the problem. If the damping term is modelled as either Rayleigh or modal damping, Eq. (18) can be expressed in the modal basis as:

$$\ddot{\boldsymbol{q}}_{\boldsymbol{i}} + \boldsymbol{c_i}\dot{\boldsymbol{q}}_{\boldsymbol{i}} + \boldsymbol{\Omega_i^2}\boldsymbol{q_i} = \boldsymbol{f_D}(\boldsymbol{t}) \cdot \boldsymbol{a_i} = \boldsymbol{f_i}(\boldsymbol{t})\ \boldsymbol{i} = 1, 2, \ldots, \boldsymbol{N_{DOF}} \tag{22}$$

$$\boldsymbol{c_i} = \begin{cases} \boldsymbol{\alpha_M} + \boldsymbol{\alpha_K}\boldsymbol{\Omega_i^2} & \textit{Rayleigh} \\ 2\eta\boldsymbol{\Omega_i} & \textit{Modal damping} \end{cases} \tag{23}$$

where η represents the percentage respect to the critical modal damping.

The idea behind this order reduction approach is that, generally, only the lower frequency modes are excited and needed to obtain an accurate approximation of the structural solution.

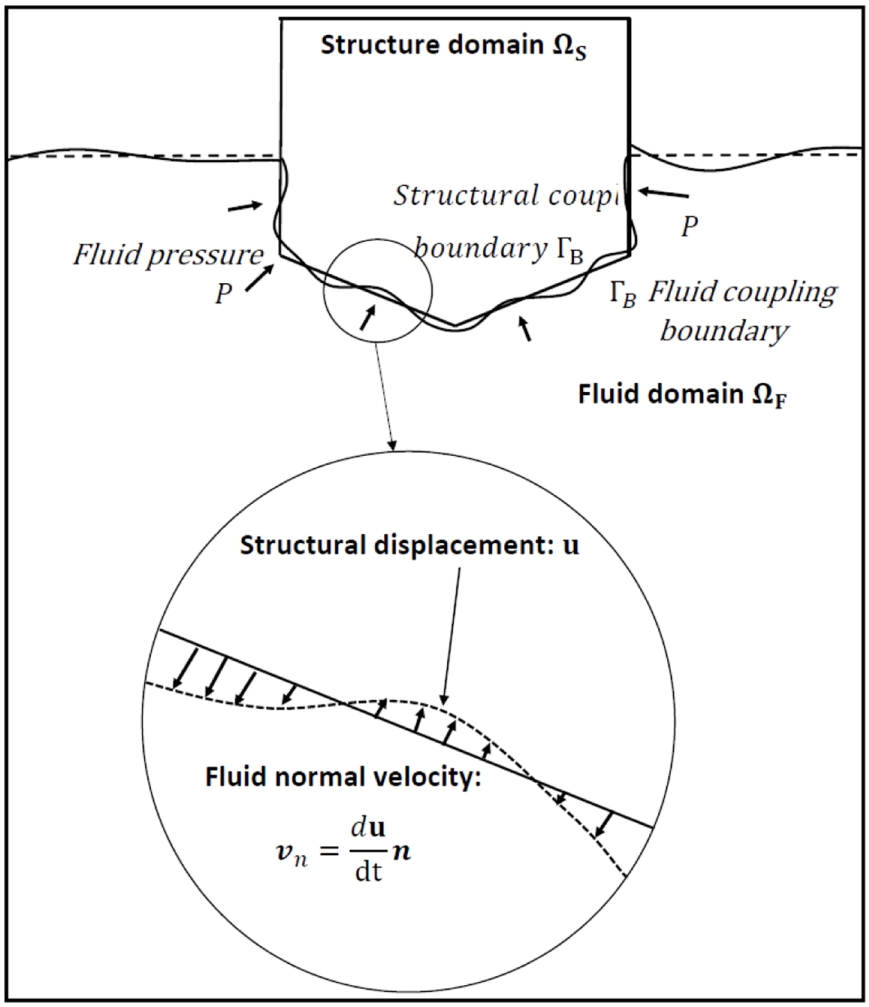

Fig. 1. Fluid-Structure interaction concept.

$$\boldsymbol{u_{MMR}}(t) = \sum_{i=1}^{N_m} \boldsymbol{q_i}(t)\boldsymbol{a_i} \approx \boldsymbol{u_D}(t)\ \boldsymbol{N_m} \ll \boldsymbol{N_{DOF}} \tag{24}$$

We define the term dynamic elastic energy $E^D(t)$ and $E^D_{MMR}(t)$ as:

$$\boldsymbol{E^D}(t) = \boldsymbol{u_D^T}\bar{\boldsymbol{K}}\boldsymbol{u_D} \tag{25}$$

$$\boldsymbol{E^D_{MMR}}(t) = \boldsymbol{u_{MMR}^T}\bar{\boldsymbol{K}}\boldsymbol{u_{MMR}} = \sum_{i=1}^{i=N_m} \frac{1}{2}\boldsymbol{\Omega_i^2 q_i^2} \tag{26}$$

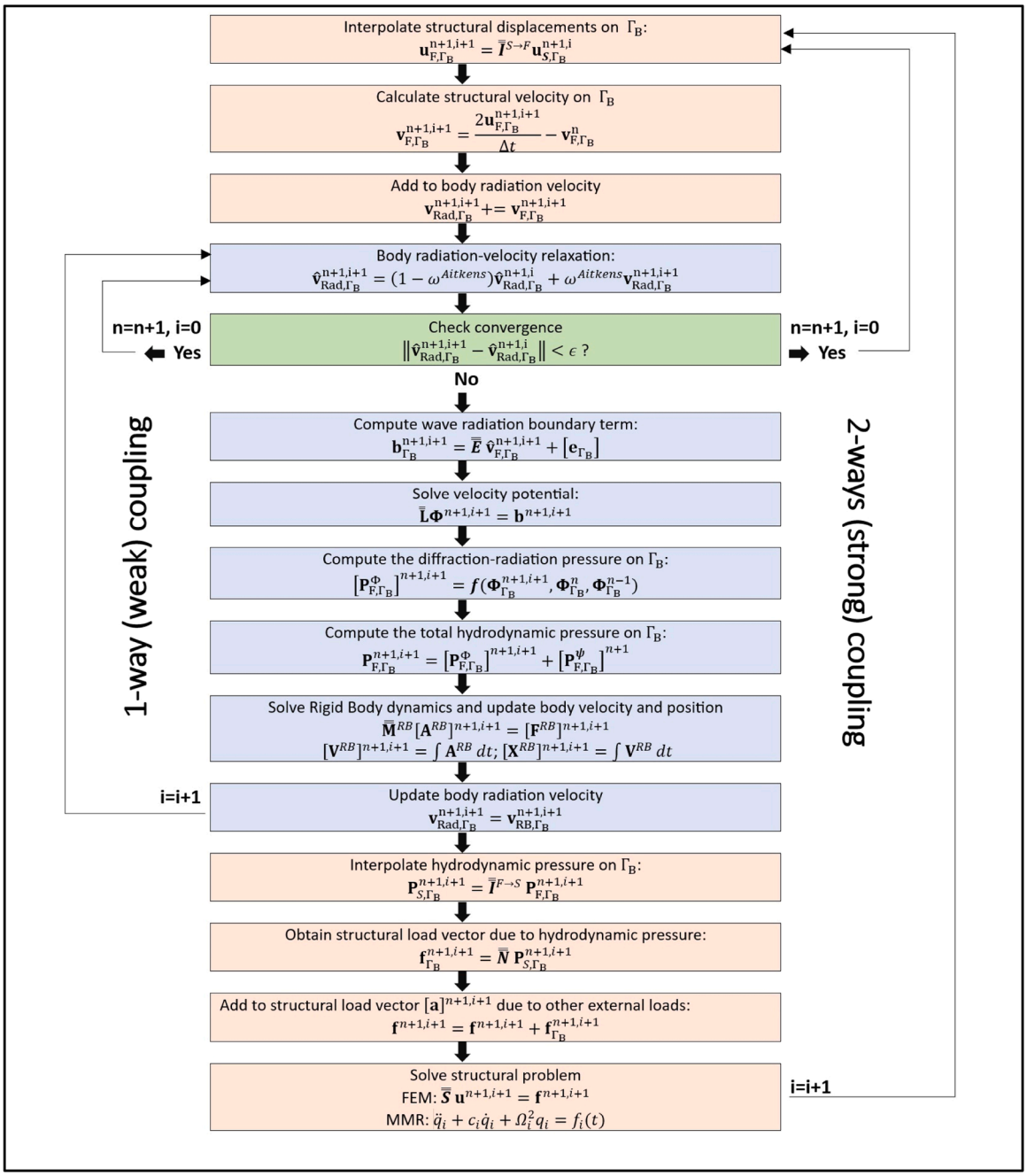

Fig. 2. Iterative scheme of the partitioned coupling.

And the dynamic energy will be used to measure the fidelity of the MMR solution to approximate the full FEM solution.

2.4. Hydroelastic coupling

The purpose of this section is to present the coupling strategy implemented to tightly couple the seakeeping hydrodynamics with the structural dynamics. The coupled problem is sketched in Fig. 1.

As presented above, the seakeeping and structural problems will be discretized using the FEM. However, it is not required to use identical discretization for the common boundary Γ_B where the interaction occurs. Spatial linear interpolators have been used in this work to transfer the fluid pressure to the structure boundary and to transfer the structural displacements to the fluid boundary.

$$\boldsymbol{P}_{S,\Gamma_B} = \overset{=F\to S}{\boldsymbol{I}} \quad \boldsymbol{P}_{F,\Gamma_B} \tag{27}$$

$$\boldsymbol{u}_{F,\Gamma_B} = \overset{=S\to F}{\boldsymbol{I}} \quad \boldsymbol{u}_{S,\Gamma_B} \tag{28}$$

where $\mathbf{P}_{S,\Gamma_B}\Delta\mathbf{u}_{S,\Gamma_B}$, $\mathbf{P}_{F,\Gamma_B}$, and $\mathbf{u}_{F,\Gamma_B}$ are the fluid pressure and structural displacements at the structural and fluid discretization over Γ_B respectively, and $\underset{=F\to S}{\mathbf{I}}$ and $\underset{=S\to F}{\mathbf{I}}$ are the corresponding interpolation matrices.

The hydrodynamic and structural solvers are tightly coupled via an iterative process where the coupling variables are interpolated back and forth from the fluid to the structural domain at the common body boundary Γ_B.

Fig. 2 shows the iterative process implemented. The iterative process allows for weak dynamic coupling, and strong dynamic coupling. In order to improve the stability and accelerate the convergence of the iterative scheme, the modified Aitken's method [38] was implemented.

2.5. OpenFAST coupling

For the coupled analysis of floating offshore wind turbines, the numerical framework developed by the authors of this work and published in [39] is used. This framework is based on SeaFEM coupled with OpenFAST via a communication interface, resulting in a time-domain aero–hydro–servo–elastic solver able to compute the combined response of floating wind systems. In its coupled solution, OpenFAST solves the aerodynamics, blades elasticity and the floater rigid-body dynamics. On the other hand, SeaFEM solves the seakeeping hydrodynamics and the mooring dynamics. The data exchange between both codes consists of the hydrodynamic loads computed by SeaFEM, and the rigid-body kinematics computed by OpenFAST. As well the wind-turbine loads from OpenFAST are received in the structural solver of SeaFEM.

The numerical framework developed by the authors of this work then is capable of combining the hydroelastic solver reported in Section 2.4 along with the abovementioned OpenFAST coupling. This results on a fully integrated load analysis framework. In this framework, OpenFAST also sends the turbine loads to SeaFEM to be included as structural loads. And SeaFEM also solves the structural response of the floater-tower taking into account the hydrodynamics, mooring, and turbine loads.

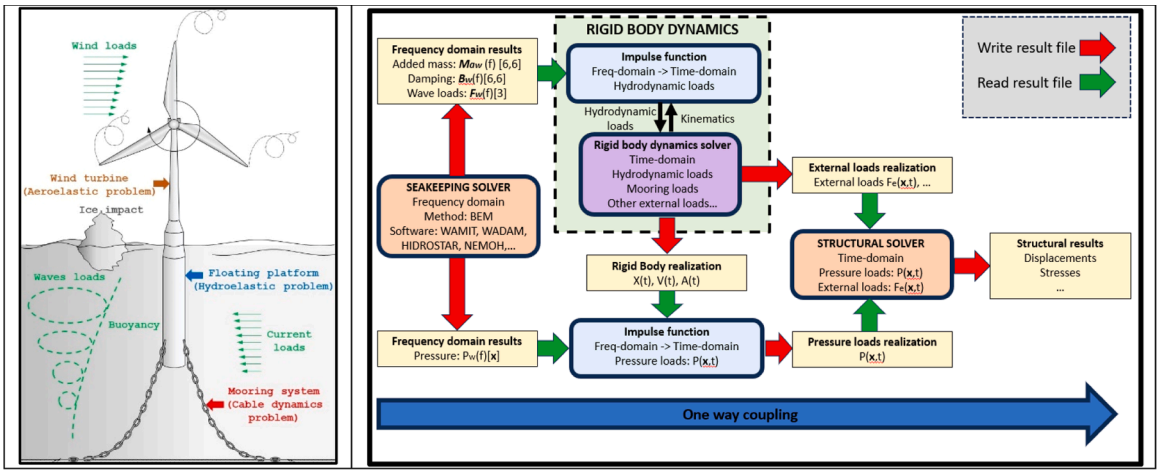

Fig. 3. Left: FOWT dynamical system. Right: Computational flow for ILA analysis using current numerical tools.

3. Integrated load analysis methodology for floating wind platforms

3.1. ILA framework

Due to the coupling between the dynamics of the wind turbine under transient wind loads and floater under irregular wave and mooring loads (see Fig. 3, left), an ILA approach is a must.

The conventional way to perform ILA analysis, including the full structure analysis, is drawn in Fig. 3 (right). The main steps are summarized as follows:

1. In the first stage, the frequency-domain seakeeping solver solves the wave diffraction-radiation problem, from where the added mass, damping, Froude-Krylov and diffraction-radiation pressure distributions and loads are obtained.
2. In order to obtain the time dependent hydrodynamic loads, those outputs need to be transformed to the time-domain for each rigid-body dynamics realization representing a load-case.
3. Later on, all external loads and the hydrodynamic pressure must be introduced into a structural solver to obtain the structural response.
4. Finally, the structural solver computes the displacements and stresses.

Several drawbacks are drawn from this methodology:

- A number of independent computational tools must be used in a serial execution.
- A large number of files and data are generated. These must be written and read.
- Only coupling in one direction is performed, limiting its use to very stiff structures (not necessarily the case of FOWTs).
- Structural dynamic simulations are a bottleneck for ILA. Often a quasistatic approach is used to reduce the computational times (hiding potential resonance/dynamic effects).

In this work, a different approach is taken (see Fig. 4). This is based on a computational framework where all external loads are simultaneously computed and applied, in the time-domain, to the structural system dynamics.

3.2. The structural solver

The structural solver is only used to transfer the structural system particulars to the computational framework. Two options are

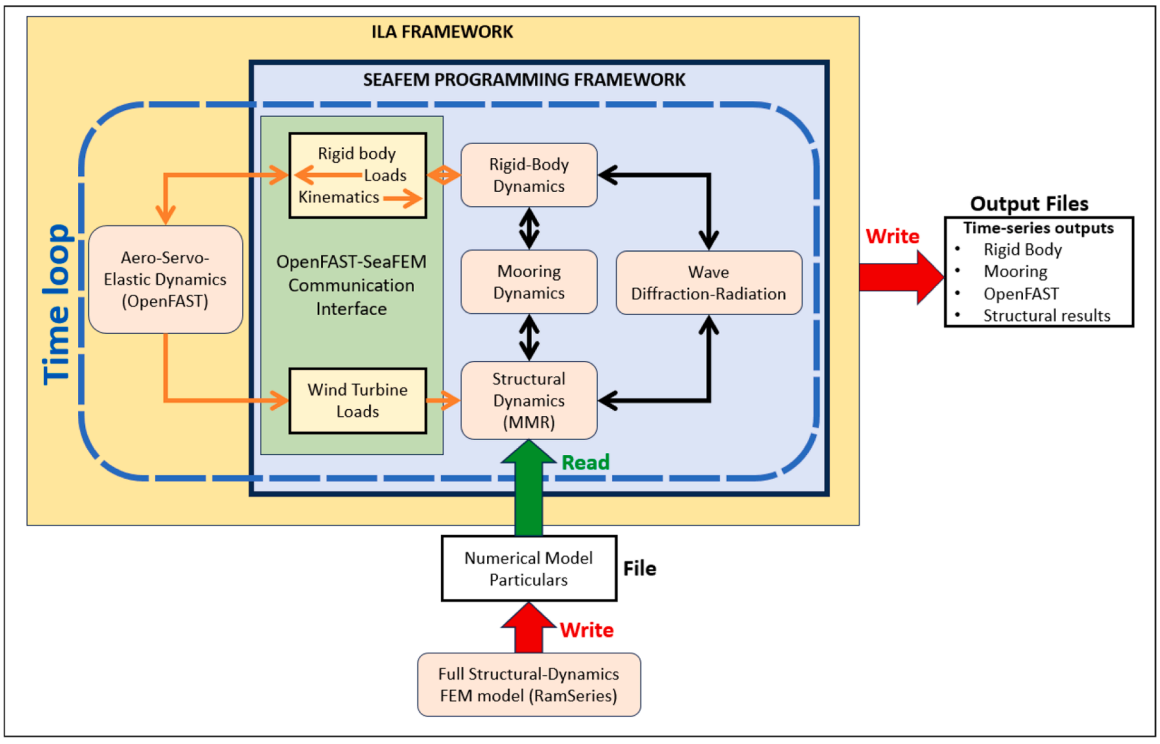

Fig. 4. ILA computational framework.

available: the full FEM model, or the MMR model (see Table 1):

The strategy drawn in Fig. 4 has a number of advantages over the one drawn in Fig. 3 (right):

- Reduces the number of interactions between different computational tools.
- Reduces the number of files to be written and read.
- Allows for strong coupling (important to account for flexibility).
- In the case of using the MMR, the size of the structural output files is significantly reduced by a factor of $O\left(\frac{N_m}{N_{DOF}}\right)$.
- All structural external loads are computed simultaneously in each time step, and straightforwardly mapped onto the structural domain.
- Minimizes the communication overheads compared to partitioned coupled strategies based on independent solvers.

When computing a large number of long structural dynamics realizations, the need of writing the time-series of the stresses leads to the problem of storing a large number of result files. These files can be large in memory size, which is not only memory demanding, but computationally demanding in terms of reading and writing tasks.

The use of the MMR largely reduces the structural output file size, since only the time-series of the modal amplitudes are reported. From these, a number of off-line computations can be performed for the structural assessment:

- Ultimate load analysis:
  - The structural energy can be quickly computed in order to identify those instants with maximum structural energy (Eq. (25)).
  - Structural displacement field reconstruction using Eq. (21) for identified extreme instants.
  - Structural stresses computation from structural displacements.
  - Identification of hot-spots.
- Fatigue damage analysis:
  - Hotspots identification.
  - Time-series structural displacement reconstruction using Eq. (21) at hot-spots.
  - Time-series structural stresses computation from structural displacements at hot-spots.
  - Fatigue damage computation from structural stresses time-series at hot spots.

4. Application example

The full-scale floating semisubmersible OC4-DeepCwind platform [40] along with the NREL 5-MW reference wind turbine [41] is used as a showcase for a high-fidelity structural analysis. To this end, a structural design of the floater and tower has been generated (hereinafter referred to as CIMNE-DeepCwind). Also, the reference mooring system consisting of three catenary lines [41], and the quadratic damping model to account for viscous effects [41] have been considered.

4.1. CIMNE-DeepCwind description

Details of the structural design are provided in the Appendix. It is worth mentioning that the purpose of this structural design is not to become a real structural solution, but to be used as an academic model to demonstrate the capabilities of the developed methodology presented in this work.

A similar mass matrix to the OC4-DeepCwind has been intended to be preserved. In Table 2, the specifications of the OC4-DeepCwind and CIMNE-DeepCwind are compared.

For a better agreement with the original concept, the external structural geometry and dimensions are kept similar, except for the central column which reaches 12 m above the sea water level (SWL), instead of 10 m as in the OC4. This implies that the tower starts at 12 m above SWL. This change was considered to improve the structural connection of the bracers with the top part of the central column.

The inner structure is mainly composed by longitudinal stiffeners, horizontal rings, and radial reinforcements. Additional

Table 1
Options for structural analysis in the ILA computational framework.

	Model	Inputs (structure particulars)	Outputs (structural results)
Option 1	FEM (RamSeries)	Mass matrix: $\mathbf{M}$ Stiffness matrix: $\mathbf{K}$ Rayleigh damping: α_M and α_K	Displacements: $\mathbf{u}(t)$ Elastic energy: $E(t)$
Option 2	MMR	Modal displacements: $a_i(x)\ i = 1,2,\ldots,N_m$ Modal frequencies: $\Omega_i\ i = 1,2,\ldots,N_m$ Rayleigh damping: α_M and α_K Modal damping: η	Modal amplitudes: $q_i(t) i = 1,2,\ldots,N_m$ Elastic Energy: $E^D_{MMR}(t)$

Table 2
Total turbine-tower-platform system particulars.

	Unit	OC4-DeepCwind	CIMNE-DeepCwind
Mass (with ballast)	kg	14,072,718	14,077,353
Downwind distance of CM	m	0.00	0.00
Lateral distance of CM	m	0.00	0.00
Vertical distance of CM	m	-9.888	-11.057
Roll inertia about CM	$kg{\cdot}m^2$	$12{,}581{\bullet}10^6$	$11{,}206{\bullet}10^6$
Pitch inertia about CM	$kg{\cdot}m^2$	$12{,}567{\bullet}10^6$	$11{,}140\ {\bullet}10^6$
Yaw inertia about CM	$kg{\cdot}m^2$	$12{,}290{\bullet}10^6$	$11{,}302{\bullet}10^6$
Ballast mass	kg	$9.6208{\bullet}10^6$	$8.5062{\bullet}10^6$

reinforcement is given in the intersections between braces and columns. The ballast is distributed within the three heave plates. An overview of the CIMNE–DeepCwind concept is presented in Fig. 5, and the scantling of the steel plates are given in Table 3. The wind turbine is included in the FEM model with the punctual masses of the NREL-5MW components. Each mass is located at its own center of mass and reported in Table 4.

The mooring solver in SeaFEM includes a dynamic FEM model described in [22] and [24]. This model has been chosen to simulate the mooring lines, whose properties are based on the OC4 model description. Each mooring line has been discretized in 64 elements.

The structural mesh used in this work is composed by 380,995 shell elements and 4 beam elements (used as auxiliary elements to impose the rotor loads). The shell element consists of a linear triangle with drilling rotations and 6 DOFs per node (three translations and three rotations) [34]. There is a total of 171,025 nodes and 1026,150 degrees of freedom. Minimum and maximum FE sizes are 0.2 and 104.7 (cm) respectively. Smallest FEs are located in areas where fatigue must be analyzed. The seakeeping computational domain mesh consists of 141,330 tetrahedral elements and 28,492 nodes. Minimum (near field) FE size is 0.25 m and maximum (far field) is 40 m. Fig. 6 shows the FEM meshes used to solve the hydro-elastic problem. The time step used in the simulations is 0.05 s.

4.2. *Modal frequency and damping in floating conditions*

The structural response of a FOWTs is largely influenced by the fore-after and side-to-side bending modes of the tower. Hence, the natural frequencies of the lower frequency modes are critical for the structural dynamics. In this section, the hydroelastic model based on MMR is used to evaluate the change in the modal frequency of lower modes in floating conditions respect to dry conditions. Also, the damping induced by the wave radiation is estimated.

The MMR technique [18] starts with the modal analysis of the FEM structural model. A modal basis of 5000 modes is computed with no restrictions. The resulting modal frequencies are in a range from 0.355 Hz to 120.497 Hz. The first 6 elastic modes are shown in Fig. 7 including their “dry” modal frequencies. The first elastic mode corresponds to the side-to-side bending mode, and the second to the fore-after bending mode.

When the platform is deployed in water, the structural displacements radiate waves (inducing fluid dynamic pressure) and cause a variation in the hydrostatic pressure. This implies changes in the modal frequency and introduces modal damping.

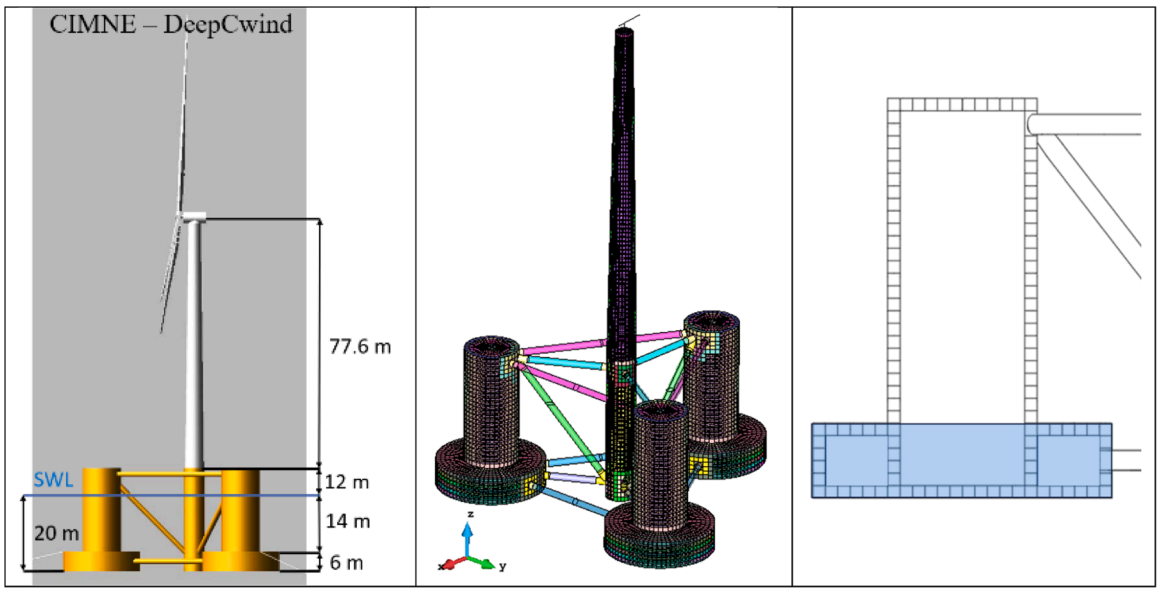

Fig. 5. CIMNE-DeepCwind. Left: main dimensions; Center: structural design; Right: ballast location.

Table 3
Structural distribution and steel plates properties.

	Thickness [cm]	Young modulus [GPa]	Poisson coefficient [-]	Density [kg/m^3]
Heave plates	3.0	210	0.3	7845
Columns	2.0	210	0.3	7845
Braces	1.75	210	0.3	7845
Tower	1.34	210	0.3	8500
Top tower plate	1.9	210	0.3	8500

Table 4
Rotor and Nacelle data of the NREL 5-MW wind turbine.

	Mass [Kg]	CM position [m]	Ixx [Kg· m^2]	Iyy [Kg m^2]	Izz [Kg·m^2]
Rotor	110,000	(-5.0, 0.0, 92.0)	35,444,000	19,011,000	19,011,000
Nacelle	240,000	(1.9, 0.0, 91.35)	0.0	0.0	1741,500

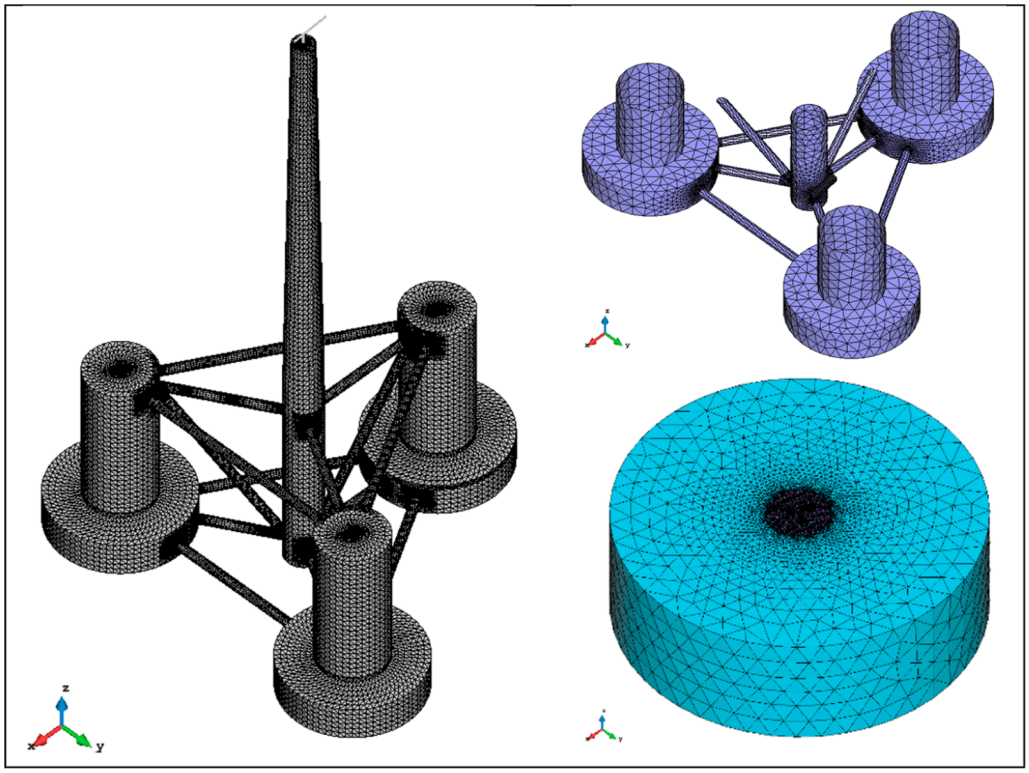

Fig. 6. FEM structural (left) and seakeeping (right) meshes.

In order to quantify the effects of the structural wave radiation, an extinction test analysis is performed for the first elastic modes assuming there is no structural damping. This test is carried out using the strong dynamic coupling and the computational framework described earlier. The platform is in hydrostatic equilibrium condition (subject to self-weight and hydrostatic pressure). The rigid body motions are kept fix and one elastic mode at a time is set free. Then its modal amplitudes will evolve until reaching equilibrium. Fig. 8 left shows the time evolution of the first elastic mode using the 2-ways (strong) hydroelastic coupling. Fig. 8 right shows a snapshot of the waves radiated during the extinction test.

Table 5 provides the change in the modal periods and the wave radiation damping for the first six elastic modes. The damping is given as a percentage of the critical modal damping. It is observed a significant change in the modal period for the first and second modes, and this must be taken into account in order to avoid potential resonance effects.

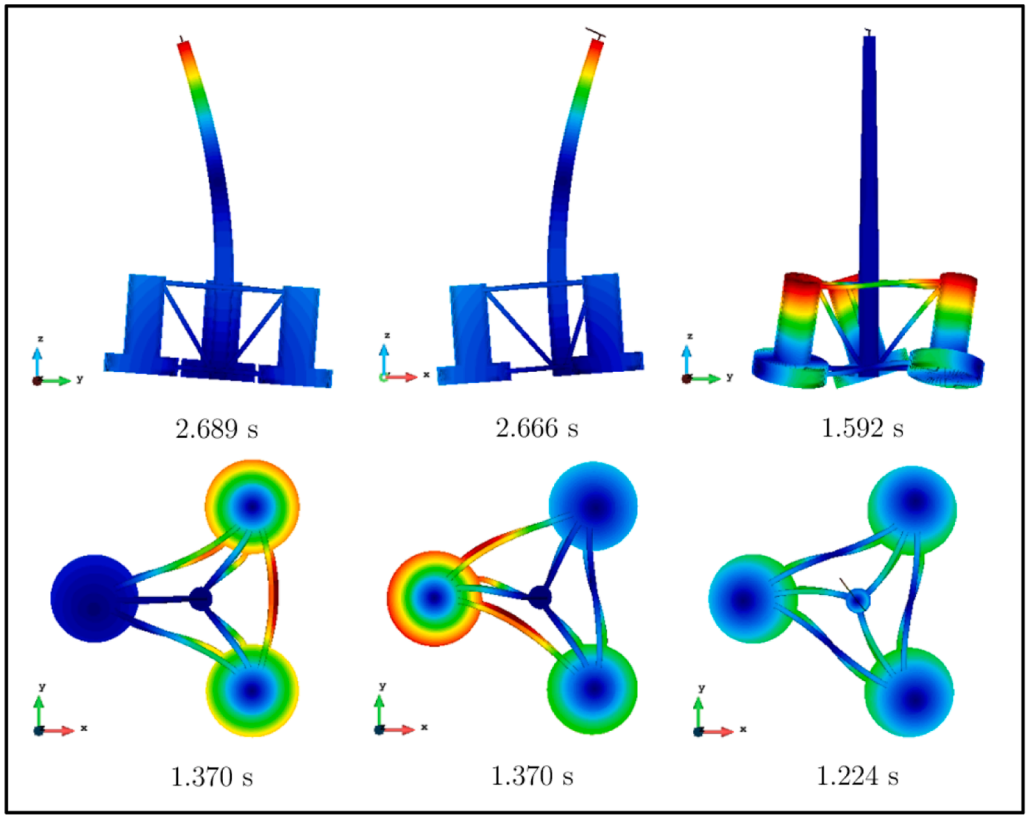

Fig. 7. First elastic dry modes and modal periods. Colorfill represents the structural displacements.

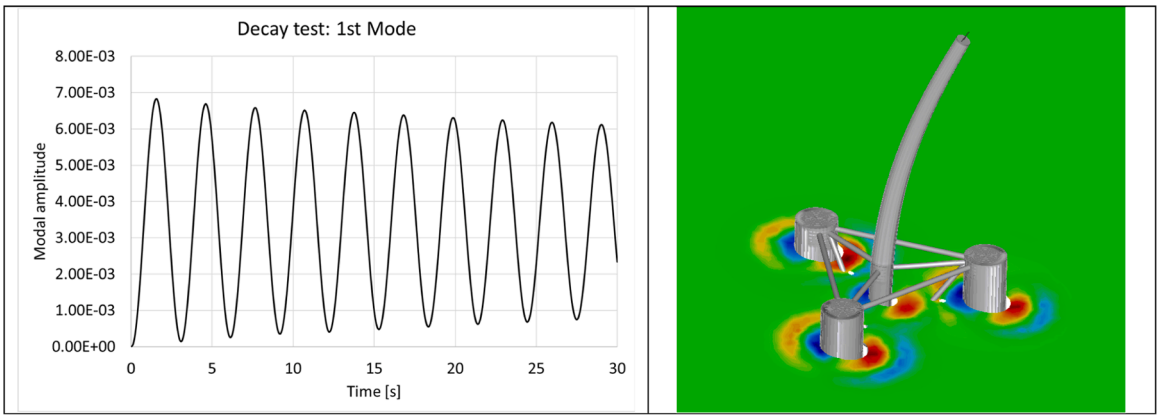

Fig. 8. Left: Extinction test for the first elastic mode. Right: Snapshot of deformed structure and radiated waves (colorfill).

Table 5
Modal periods and damping for the first six elastic modes.

	1st Mode	2nd Mode	3rd Mode	4th Mode	5th Mode	6th Mode
Dry period [s]	2.689	2.666	1.592	1.370	1.370	1.224
Wet period [s]	3.055	3.033	1.769	1.410	1.410	1.265
Wave radiation damping [%]	0.462	0.456	0.968	0.051	0.049	0.079

4.3. RAO analysis in irregular waves

4.3.1. Rigid body response

As a first verification, the rigid-body response is compared with the one from the OC4-DeepCwind model. To do so, first a time–domain simulation using a white noise head wave spectrum is performed in the absence of wind and currents. The response amplitude operators are obtained considering the wind turbine in parked condition.

SeaFEM standing alone is used to compute the RAOs for the CIMNE-DeepCwind. These are compared with the OC4-DeepCwind response according to the OC4 project, phase II load case 2.6 [42]. Fig. 9 compares the results with those published by NREL. Only the frequency band excited by the waves is provided in the plots.

As expected, due to the different characteristics of the two models, slight discrepancies are found. However, a reasonable agreement is observed between the OC4-DeepCwind and CIMNE-DeepCwind. Additionally, consistency is found in the natural frequencies obtained from decay tests with both models. Table 6 compares the natural periods computed for the CIMNE-DeepCwind and the OC4-DeepCwind provided in [43].

4.3.2. Modal response amplitude operators

Response amplitude operators for the different modal displacement fields, hereinafter referred to as Modal Response Amplitude Operators (MRAOs), are calculated for monochromatic waves using a white noise spectrum propagating in the longitudinal direction. The range of wave periods goes from 0.5 s to 100 s, and a total of 371 wave frequencies have been computed. The structural damping is set to 1% of the modal damping. The second elastic mode corresponds to the fore-after bending mode of the tower. Since the waves propagate in the longitudinal direction, this mode is expected to have a relevant contribution to the elastic energy. Hence, although MRAOs have been obtained for all modes, this analysis will focus on that mode.

Fig. 10 compares the MRAOs for the second mode computed using a quasistatic (QS), weak and strong dynamic couplings. As expected, near the mode resonance frequency, the quasistatic approach fails to recover the dynamic behaviour. And for the dynamic solutions, the resonance peak moves due to the change in the modal frequency from dry to wet conditions. Also, away from the resonance frequency (below 0.1 Hz), the three approximations provide similar results, having a peak at the pitch natural frequency. In the case of one-way coupling, since structural wave radiation is ignored, the resonance occurs at the dry frequency instead of the wet frequency, resulting in a less accurate representation of the structural response.

Given a wave energy spectrum $S_w(\omega)$, one can obtain the structural energy spectrum $S_m(\omega)$ for mode "m'' as:

$$S_m(\omega) = \Omega_m^2 \; S_w(\omega) \; MRAOs(\omega)^2 \tag{29}$$

The zero order moment (E_m^0) of $S_m(\omega)$ is given by.

$$E_m^0 = \int_0^\infty S_m(\omega) d\omega \tag{30}$$

E_m^0 is an indicator of how much elastic energy mode "m'' will absorb under a seastate given by $S_w(\omega)$. Fig. 11 compares $E_{m=2}^0$ for a JONSWAP spectrum with $H_S = 1m$. It is observed that the modal energy increases significantly for Tp values close to the mode's resonance frequency. However, the quasi-static approach is unable to capture this effect. Moreover, the change in modal frequency from dry to wet conditions also have a significant impact for T_p around the modal resonance. The modal energy E_m^0 can be used also as an indicator to select most excited modes and further reduce the modal basis. Moreover, the total energy $E^0 = \sum_m E_m^0$ can be also used as an indicator to select those extreme wave conditions inducing largest values of E^0.

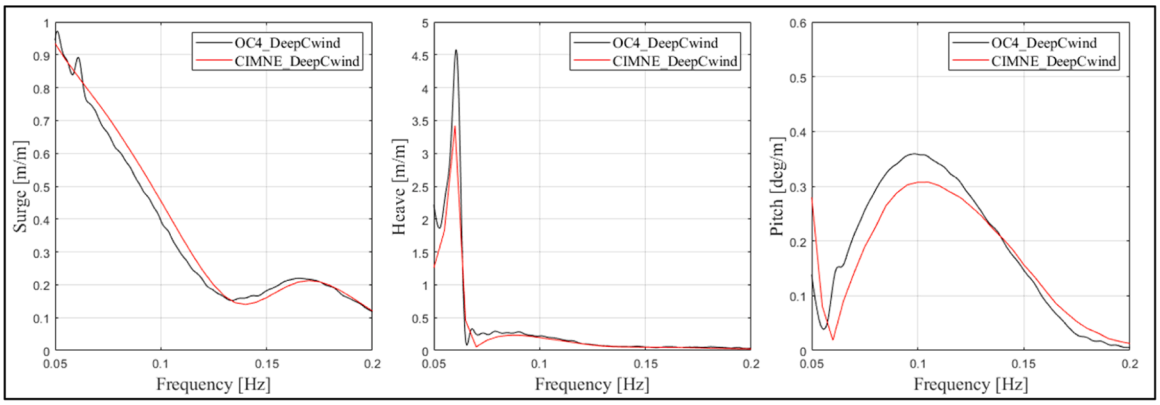

Fig. 9. RAOs comparison without wind (OC4DeepCwind – CIMNE-DeepCwind).

Table 6
Platform natural periods.

	OC4-DeepCwind	CIMNE-DeepCwind
Surge	107.52 s	109.54 s
Sway	113.63 s	109.96 s
Heave	17.24 s	16.70 s
Roll	27.03 s	23.76 s
Pitch	27.02 s	23.70 s
Yaw	83.33 s	76.50 s

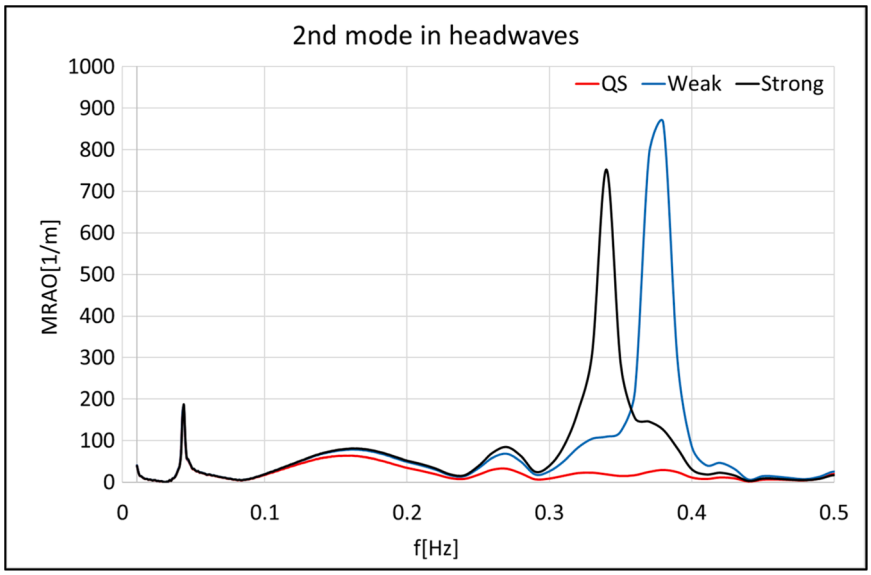

Fig. 10. MRAOs comparison for 2nd elastic mode.

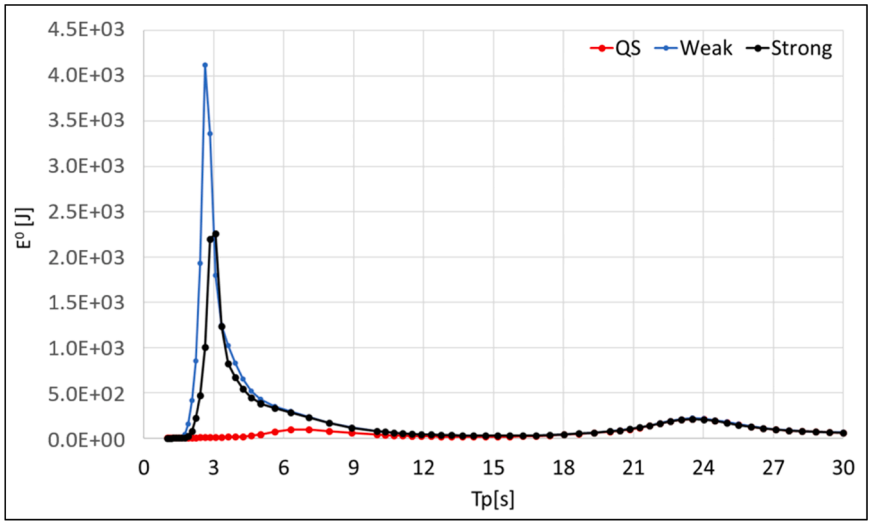

Fig. 11. Structural energy versus wave peak period for 2nd elastic mode. Wave spectrum: Jonswap. Hs=1 m.

4.4. Second-order wave loading and structural resonance

In marine and offshore engineering, it is a common practice to assume that structures are stiff enough so a quasistatic response to wave loading can be also assumed. However, in floating wind, the presence of the wind turbine on top of a slim tower makes lower

modal frequencies to get closer to the wave loading frequencies.

SeaFEM enables the time-domain solution of wave diffraction and radiation up to the second order, allowing for the modeling of both Airy waves and second-order Stokes waves. The second-order equations are derived by applying a Taylor series expansion to the free surface and body boundary conditions. A perturbed solution, based on the Stokes wave approximation, is then applied to the velocity potential, free surface elevation, and floater motion. More details can be found in [20,22,24]. In this section, these capabilities are utilized to assess structural resonance under higher-order wave excitations.

4.4.1. Monochromatic wave

In this section, we analyze the structural response under a monochromatic wave with wave period $T = 6.066$ seconds and one meter amplitude. This wave period corresponds to the double of the wet modal period for the second mode. Hence, the second order component of the wave is expected to induce resonance effects. The purpose is to compare the structural energy for the QS, and the weak and strong coupling schemes.

Fig. 12 shows the instantaneous elastic energy, computed by the MMR5000 model, under first and second order wave loading. In Fig. 12 left the first order response shows that the dynamic effect is still relevant for this wave period. This makes the QS coupling to underpredict the structural energy, while little difference is observed between the weak and strong couplings. Fig. 12 right shows the structural energy also considering the second order loading. In this case, the QS solution is similar to the first order, so no resonance

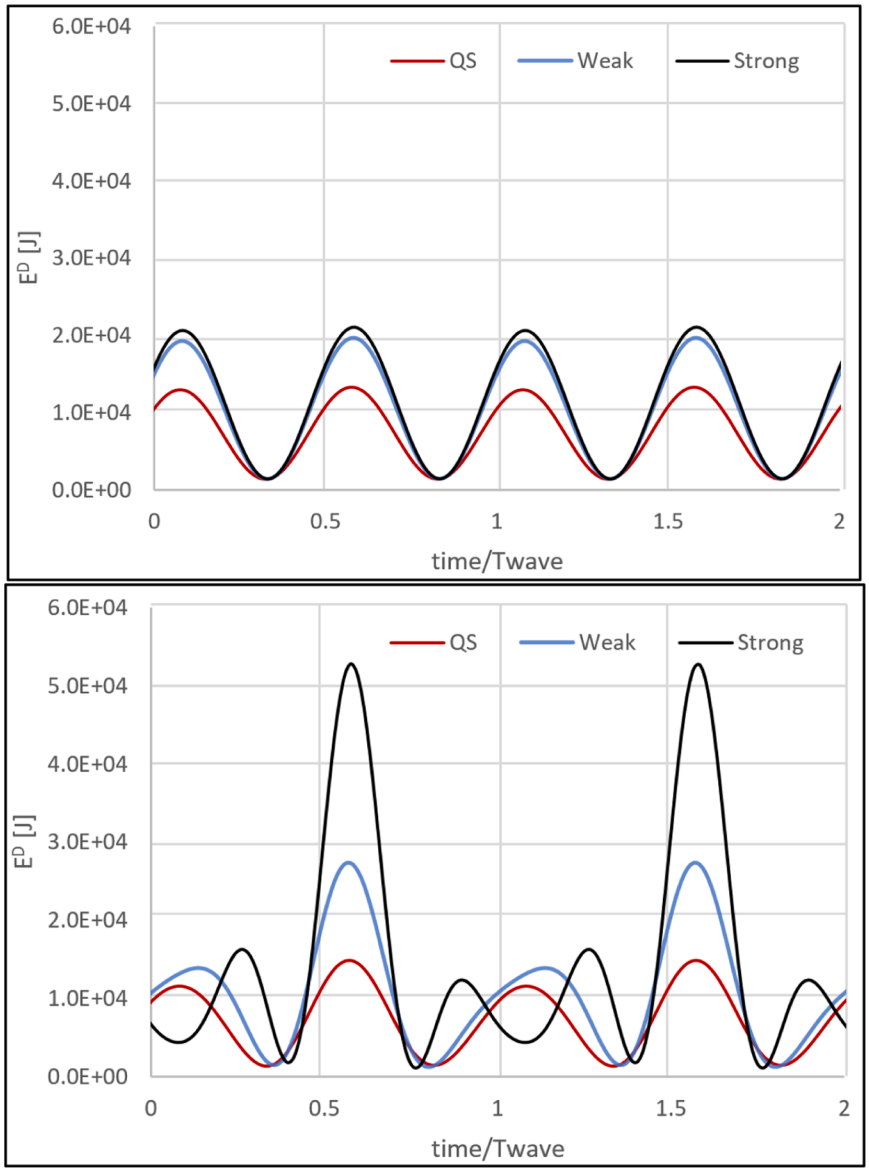

Fig. 12. Instantaneous elastic energy under first (left) and second (right) order monochromatic wave.

effect is shown as expected. The weak solution shows some near resonance effect, but still underpredicts the resonance effect compared to the strong.

This case study points out the importance of using, not only a dynamic coupling, but also a 2-ways dynamic coupling when wave load frequencies are in the near resonance range. And as a consequence, it is important to quantify the change in the modal frequency from dry to wet conditions.

4.4.2. *Irregular waves*

In this section, we analyze the structural response under irregular waves. The irregular waves are modeled using a Jonswap spectrum with mean wave period $T_m = 6.066$ seconds and significant wave height $H_S = 3$ meters. This wave period corresponds to the double of the wet modal period for the second mode. Hence, the second-order components are expected to induce resonance effects. The purpose is to compare the structural energy for the quasistatic QS, weak, and strong coupling schemes.

Fig. 13 shows the instantaneous elastic energy, computed by the MMR5000 model, under first and second order wave loading. In Fig. 13 (top), the first-order response shows that the dynamic effect is still relevant for this wave period. This makes the QS coupling to underpredict the structural energy. Significant differences are observed between the weak and strong dynamic couplings. Fig. 13 (bottom) shows the elastic energy also considering the second-order loading. In this case, the QS solution shows some differences to the first-order. The weak coupling shows some near resonance effect but large differences are observed when compared to the strong coupling.

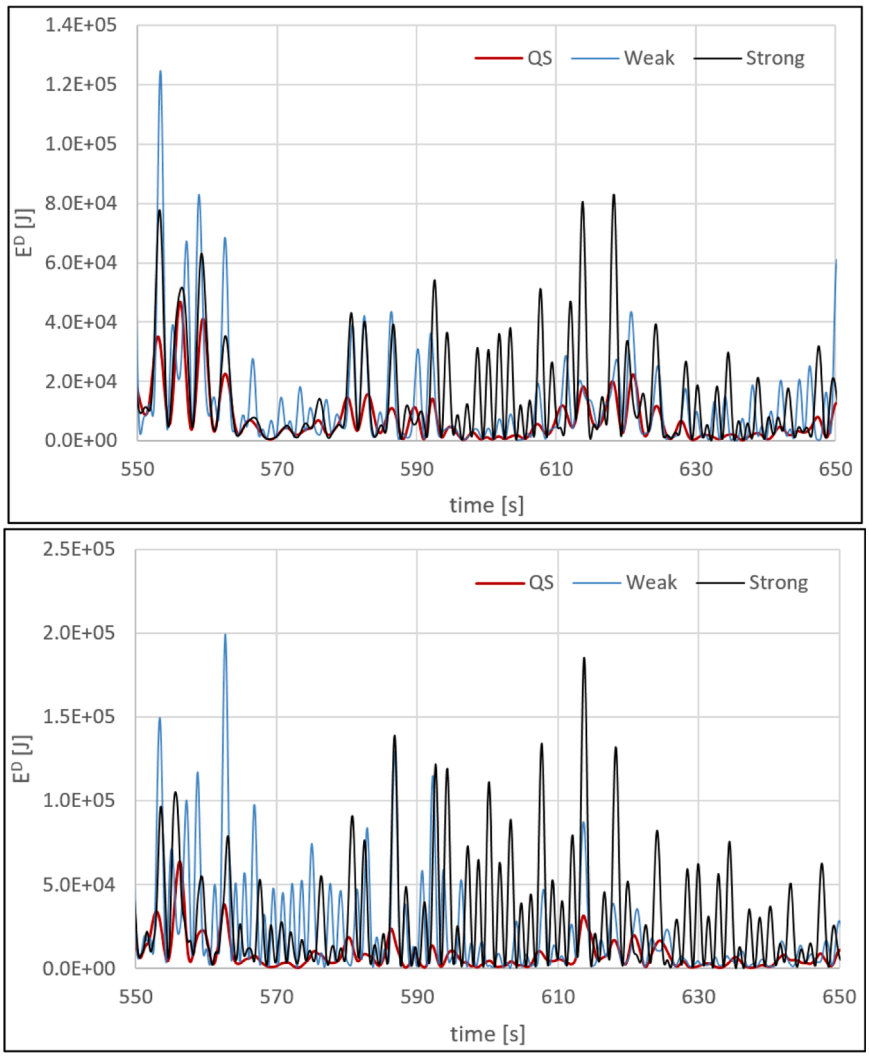

Fig. 13. Instantaneous elastic energy under first (top) and second (bottom) order irregular waves. Wave spectrum: Jonswap, $_{Hs}$=3 m, T_m=6.066 s.

4.5. MMR versus FEM

4.5.1. Hydrostatic equilibrium analysis

Although the MMR has been proposed to reduce computational times of dynamic analysis, the structural solution under hydrostatic equilibrium is compared using FEM and MMR. The comparison of the structural displacements between the FEM solution and the MMR technique using 5000 modes is presented in Fig. 14. The consistency of the structural model order reduction solution is tested, being able to accurately approximate the high-fidelity FEM solution.

4.5.2. DLC 1.6: production design

The load case 1.6 for production operation defined in the Bureau Veritas standards [44] is tested. This condition consists in a normal turbulence wind combined with a severe sea state. The detailed parameters used for the simulation are computed according to the IEC standards [45]. The weather database used is obtained from the European project Corewind D1.2 [46] for the site location in Morro Bay (California). In Table 7 is given a summary with the parameters used to define the analyzed loadcase. A simulation time of 800 s using the weak hydro-elastic coupling for 5000 modes is performed in only-waves and wind-wave conditions.

According to the chosen site location, the irregular sea-state is defined with a Jonswap wave spectrum using a significant wave height of 6 m and a mean wave period of 14 s. A number of 100 waves is used for the spectrum discretization. The wave period range goes from 5 s to 35 s to cover the energy spectrum. The turbulent wind field is generated with TurbSim for a wind speed of 14.8 m/s at the hub height. In order to be able to compare the MMR and FEM model, the same structural damping must be used. Hence, the Rayleigh damping is used with $\alpha_M = 0$ and $\alpha_K = 2 \cdot 0.01 \cdot \Omega_1^{-1}$, where Ω_1 is the first elastic modal frequency. The equivalent modal damping is $c_i = 2\eta_i\Omega_i$, where $\eta_i = 0.01 \cdot \Omega_i \cdot \Omega_1^{-1}$ is the percentage of the critical damping. To quantify the relevance of the dynamic effects, its single contribution is analyzed by subtracting the static loads during the simulations.

4.5.2.1. Wave only analysis. The structure subject to only-wave loads is analyzed using the weak dynamic coupling. The purpose of this study is to verify the consistency of the MMR approach with respect to the high-fidelity FEM solution, being the fully coupled solution not necessary. An 800 s simulation has been carried out, where the initial 200 s are discarded due to transients/initialization effects.

Fig. 15 compares the dynamic energy when using FEM and MMR with 1000 and 5000 modes. As well the dynamic solutions can be compared with the quasistatic FEM approach. The MMR solution agrees with the FEM one, proving that even with a modal basis of 1000 modes is enough to capture most of the structural dynamic energy. From the instantaneous energy plots, it is possible to detect the instant where the structure is most stressed.

Fig. 15 (top), shows the different solutions in the total analyzed time, and (bottom) shows the local maximums of dynamic energy for the last time range of 100 s. Table 8 gives the percentages for the four maximum peaks in the dynamic and quasistatic analysis. The percentages are computed with respect to the dynamic FEM solution. The signal peaks are well predicted with the modal approximations, retaining over the 95% in overall even for the 1000 modes MMR. It is observed a better approximation with the dynamic MMR rather than with the FEM quasistatic solution. The MMR results in a closer approach since capturing the higher elastic energy concentration in the first modes when performing dynamic analysis.

Table 9 shows the computational cost of the different solvers used in the present one-way simulations. In this case, both structural models (FEM and MMR) were used for comparison purposes. It is observed that the structural FEM is the most expensive part to compute, and the MMR5000 is about 10 times faster than the FEM. The table also includes the computational times required for a two-ways coupling. OpenMP with parallel execution in 4 CPUs has been used. The CPU unit used was the AMD Ryzen Threadripper PRO

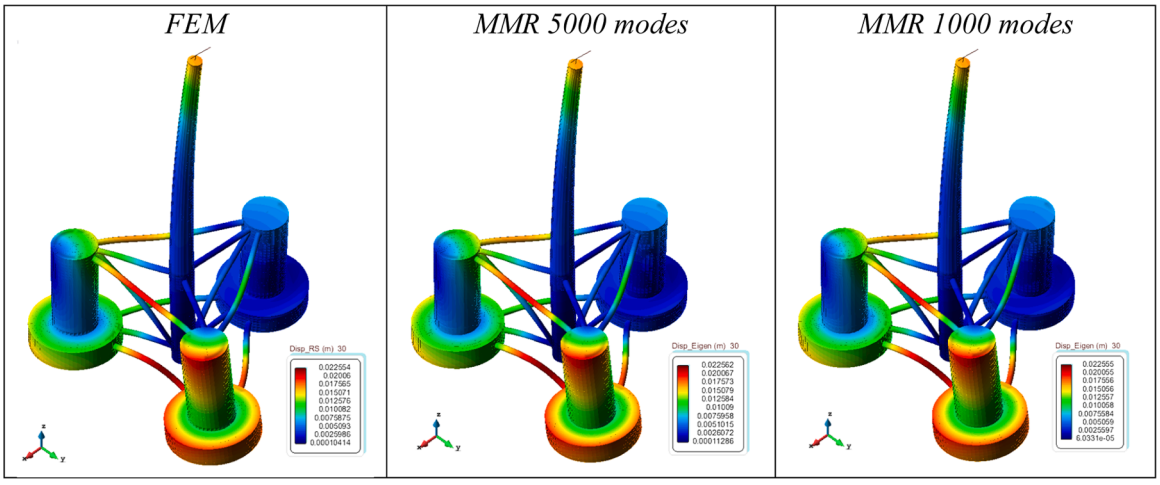

Fig. 14. Structural displacements (amplified x200).

Table 7
Production design load case 1.6.

DLC	1.6 Production design
Site location	Morro Bay (California)
Depth	200m
System condition	Intact
Wind	Speed: 14.8 m/s (hub height) Normal turbulence
Waves	Severe Spectrum: Jonswap Hs=6m T=14 s Direction: 0° Spreading: Unidirectional

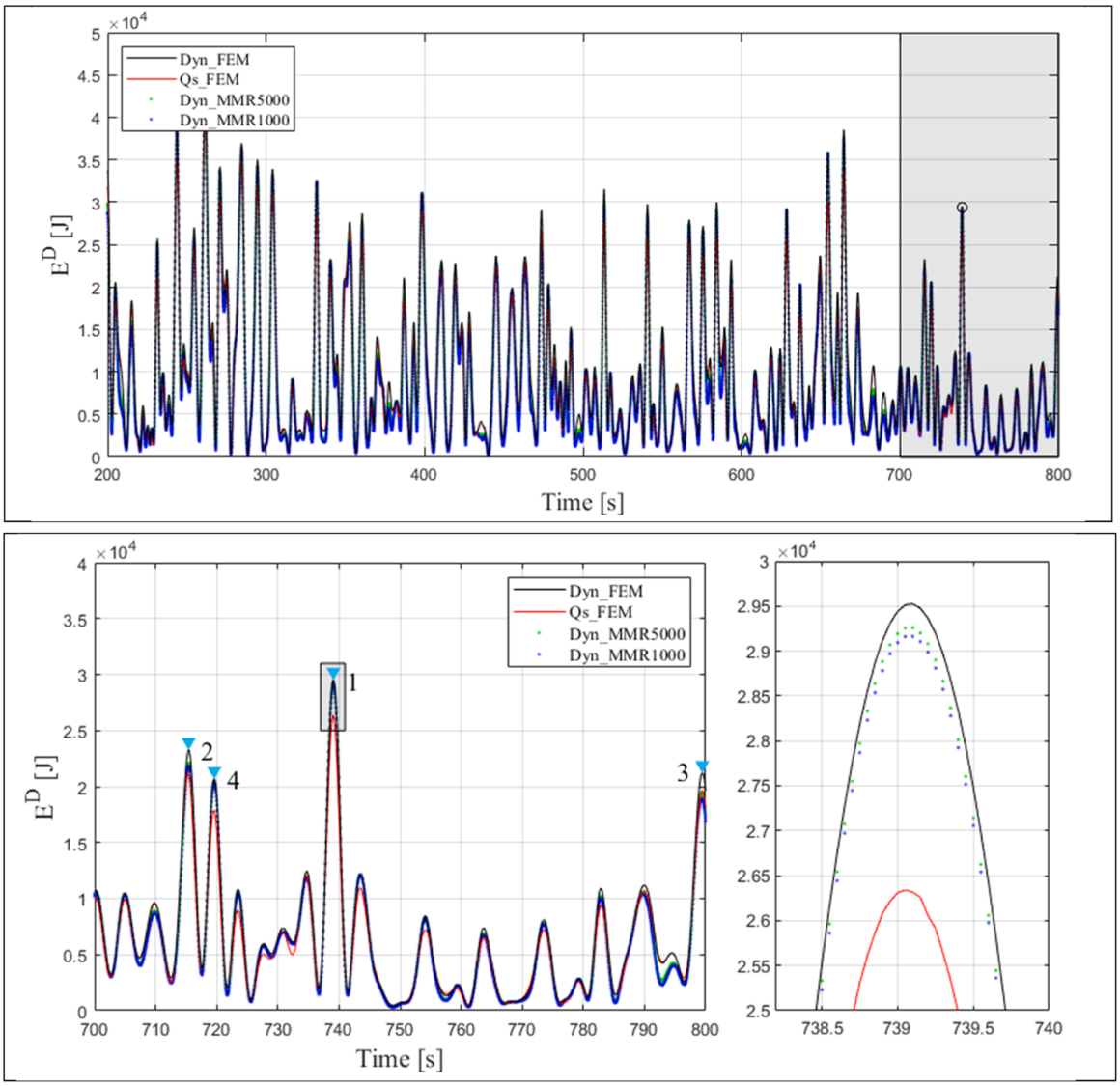

Fig. 15. Instantaneous E^D and plots, top: total time range and bottom: bounded time range and maximum peak.

5995WX 2.70 GHz.

The present methodology allows to identify the potential hotspots for fatigue damage. This can be done simply by looking for the maximum stress points at the most energetic time instants. Once a time instant is selected, the stress solution is computed offline. The

Table 8
Percentage of the E^D with respect to the dynamic FEM analysis.

Analysis type	Dynamic			Quasistatic		
Number of modes	FEM	MMR 5000	MMR 1000	FEM	MMR 5000	MMR 1000
Peak 1	100%	99.07%	98.74%	89.09%	88.19%	87.87%
Peak 2	100%	95.05%	93.87%	91.20%	86.26%	85.10%
Peak 3	100%	92.31%	89.93%	92.59%	84.90%	82.52%
Peak 4	100%	99.16%	98.83%	86.79%	85.97%	85.63%

Table 9
Computational cost.

Solver	Computational time/Simulation time	
	One-way	Two-ways
Rigid Body+Dynamic Mooring (FEM):	1.51 s/s	2.19 s/s
Wave diffraction-radiation	0.93 s/s	1.27 s/s
Structural FEM	5.48 s/s	66.26 s/s
Structural MMR 5000	0.47 s/s	5.29 s/s
Structural MMR 1000	0.10 s/s	1.06 s/s

full displacement field is first obtained by linear combination of the modal displacements. And afterwards, the strains and stresses are computed using the material properties.

In this case study, computing the stresses for a single time instant across all finite elements takes approximately 0.1 s. Given a one-hour simulation with an average wave period of 14 s, the number of local maximums would be approximately 257 time instants (3600/14). Consequently, computing offline the dynamic stresses for the entire structure at these critical time instants would take approximately 25 s.

In Fig. 16 (left) is given a snapshot of the simulation at its maximum structural dynamic energy instant. The free surface elevation and stress field in the whole structure are shown. The structure deformations are amplified by 150. A closer view of the stress field with the position of the element with maximum stress is pointed in Fig. 16 (right).

Table 10 provides the values of the most energetic modes and its cumulative energies. The fore-aft bending mode, second elastic eigenmode, retains the higher structural energy.

Fig. 17 left shows the element of maximum stress in the second mode for the time instant of maximum dynamic energy (hotspot). This is found in the reinforcement between the braces joint and the main column. The stress time-history at this hotspot is obtained offline for the time range of 100 s and compared to the dynamic energy. Close correlation is observed between the stress and energy peaks signals. This confirms the validity of the methodology based on the structural energy for the identification of those critical instants and potential hotspots.

The average time to compute the stresses at the hotspot in one time step is 0.0002 s. Then, for a one-hour simulation with a time step of 0.05 s, the stresses time-history at one hotspot can be computed in about 14.4 s. The computational time to obtain the stresses

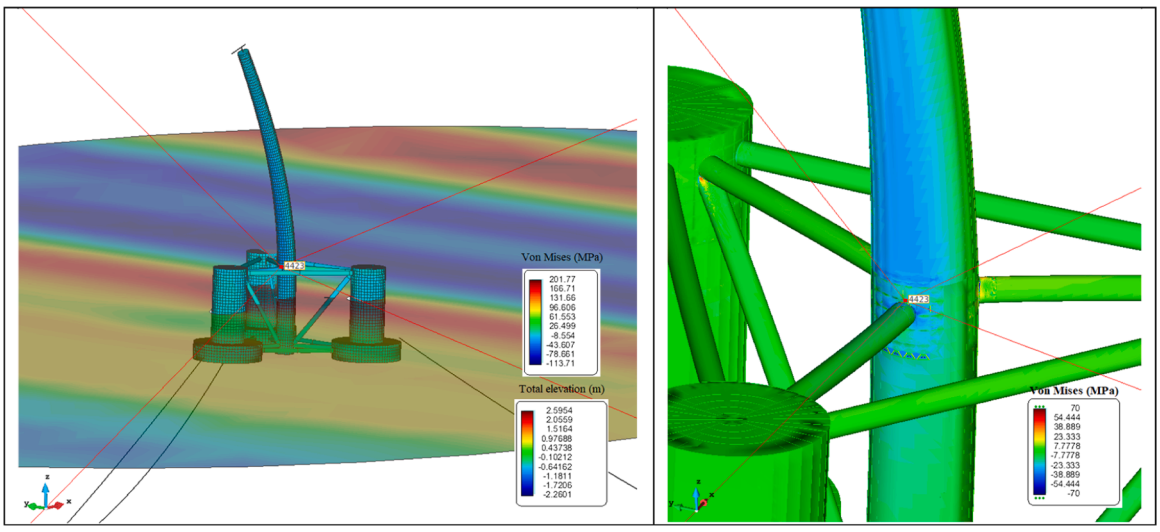

Fig. 16. Left: stress field and deformation in critical condition (def x150). Right: close-up view of the stress field.

Table 10
Energy distribution and cumulative energies from the most energetic modes.

Mode	Modal E^D [J]	E^D [%]	Accumulated E^D [%]
2	6375.66	71.51%	71.51%
11	450.28	5.05%	76.56%
13	378.14	4.24%	80.80%
17	160.74	1.80%	82.60%
866	158.02	1.77%	84.37%

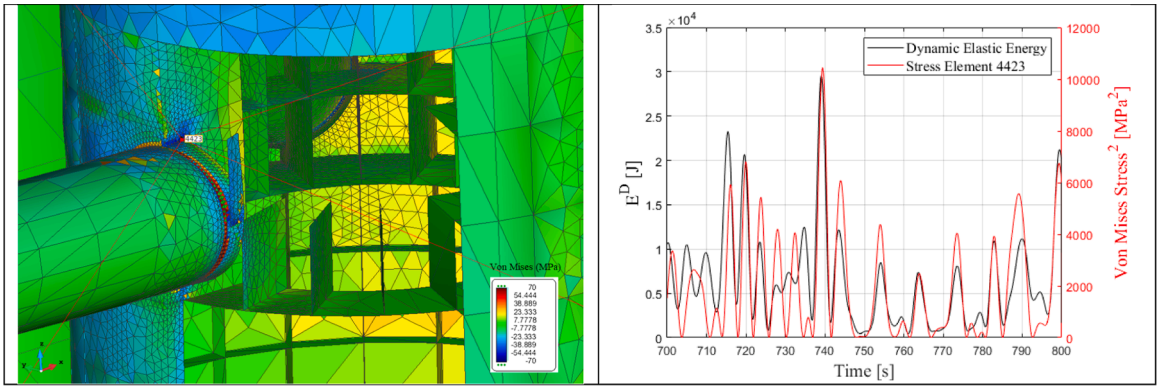

Fig. 17. Stress filed and location of maximum stress hotspot (left). Instantaneous squared Von Mises stresses at hotspot element and structural dynamic energy (right).

time-history will grow/decay linearly with the number of hotspots and time steps. When computing the stresses offline the computational effort in the postprocess can be reduced. This is done by reducing even more the modal basis after averaging the modal energy and discarding the least energetic eigenmodes.

4.5.2.2. Wind-Wave analysis. The structure subjected to wind and wave loads is analyzed next using the weak dynamic coupling. Fig. 18 compares the dynamic energy when using FEM and MMR. The MMR solution agrees with the FEM one.

Below, Table 11 gives the percentages for the local maximum peaks. The percentages are computed with respect to the dynamic FEM solution. Agreement is found in the modal approximations, retaining over the 90 % of the dynamic structural energy.

As seen, the dynamic component is also relevant when computing load-cases with wind. In Fig. 19, is plotted the E^D computed by the FEM solution in the dynamic analysis for both conditions.

In Fig. 20. (left) is given a snapshot of the simulation for the wind-wave condition at its maximum structural energy instant. The free surface elevation and stress field in the whole structure are shown. The structure deformations are amplified by 150. The position of the elements with maximum stresses is pointed in Fig. 20. (right), coinciding with previous analyzed loadcase for the element 4423. As observed, the potential hotspot suffers from compression stresses, according to the fore-aft bending mode. Table 12 provides the time-averaged energies of the most energetic modes and its cumulative percentage. The most excited eigenmode has a less energetic contribution compared to the only-waves condition.

From the stress field at the critical loadcase condition, it is possible to identify the region associated with the highest fatigue damage, as is the case of the tower base caused by the tower's bending moment [12] or the intersection between structural members. A detailed view of the hotspot location, found in the reinforcement between the braces joint and the main column at the tower's base is given in Fig. 21. The real-time stresses at this point are obtained offline for the time range of 100 s. Again, a strong correlation is observed between the stress and structural FEM energy signals.

5. Conclusions

This work has presented a numerical framework for fully coupled ILA of floating structures in general, and for floating wind platforms in particular. This framework is built within the SeaFEM seakeeping hydrodynamics framework, where SeaFEM has been enriched with a structural solver and coupled with OpenFAST.

The structural solver implemented allows for using two options: the full FEM system, or a ROM based on the MMR technique. The consistency of the MMR has been verified comparing against FEM solution, finding a very good agreement in all analyzed conditions. For the present application, a modal basis of 5000 eigenmodes has been considered to accurately recover the elastic structural energy. The MMR implies a large reduction in the number of structural degrees of freedom (dof) from 1026,150 dofs of the FEM model to 5000 modes. Using the MMR 5000 results in a reduction of approximately a 90 % in the computational time of the structural solver with respect to the full FEM. And there is still room for further reduction of the modal basis if only most energetic modes are considered. And

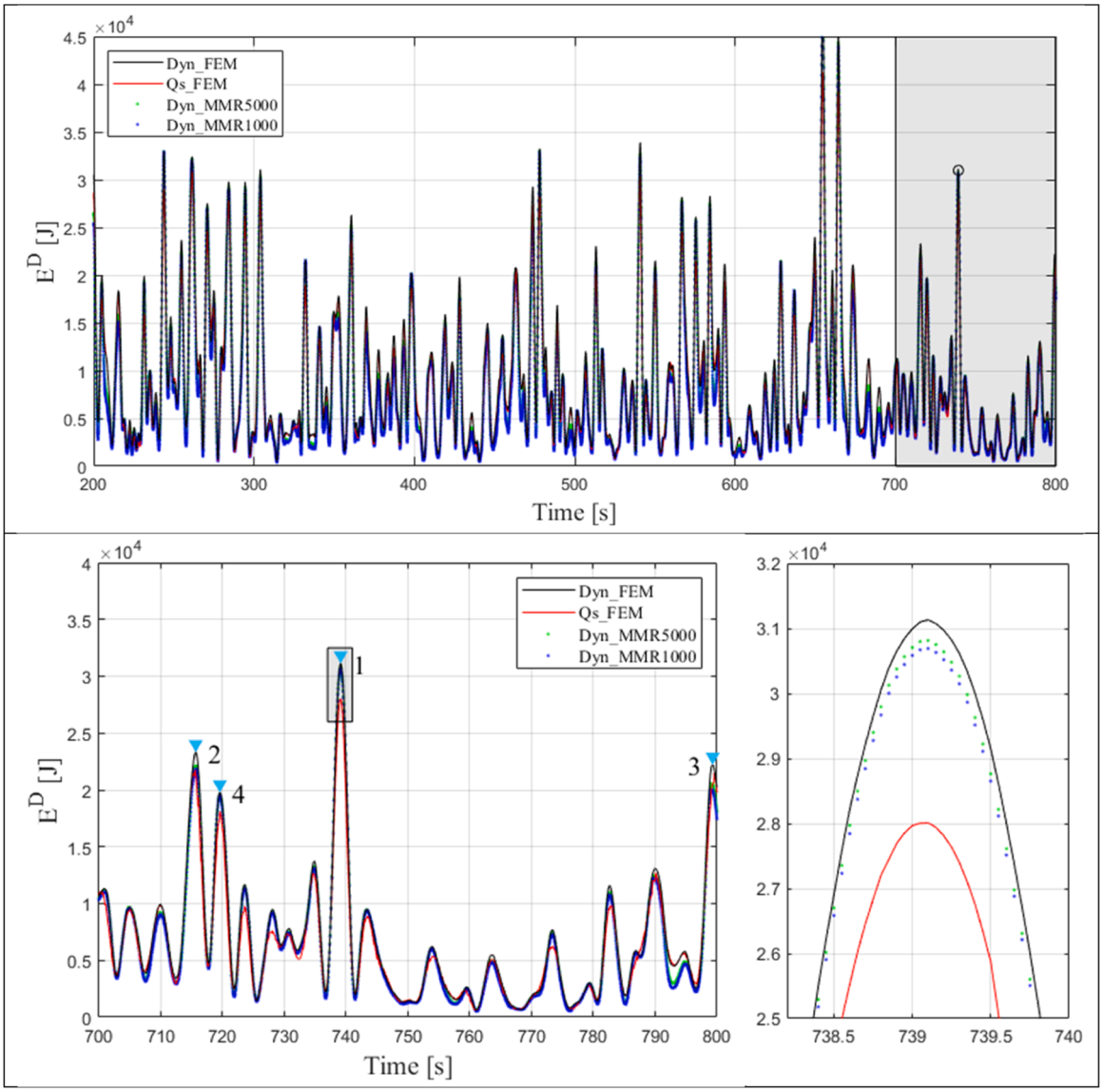

Fig. 18. Top: Instantaneous E^D plots; Down: 100 s time range and maximum peak.

Table 11
Percentage of the E^D with respect to the FEM dynamic analysis.

Analysis type	Dynamic			Quasistatic		
Number of modes	FEM	MMR 5000	MMR 1000	FEM	MMR 5000	MMR 1000
Peak 1	100%	98.96%	98.57%	89.92%	88.90%	88.65%
Peak 2	100%	94.78%	93.53%	95.22%	89.90%	88.67%
Peak 3	100%	92.72%	90.43%	91.81%	84.54%	82.21%
Peak 4	100%	99.04%	98.64%	87.75%	86.81%	86.40%

this reduction will be proportional to the number of modes used.

The MMR approach allows for the offline computation of the structural displacements and stresses. This are computed from the modal amplitudes and the modal basis. Then, the instantaneous structural energy allows for the detection of the critical time instants. At these, the hotspots of maximum stresses can be identified. This avoids the need to compute the stresses over the full structure along the whole simulations. Instead, the structural response can be obtained over the whole structure at critical time instants, and for every time step at specific hotspots. This implies a more precise analysis and a large reduction of output data.

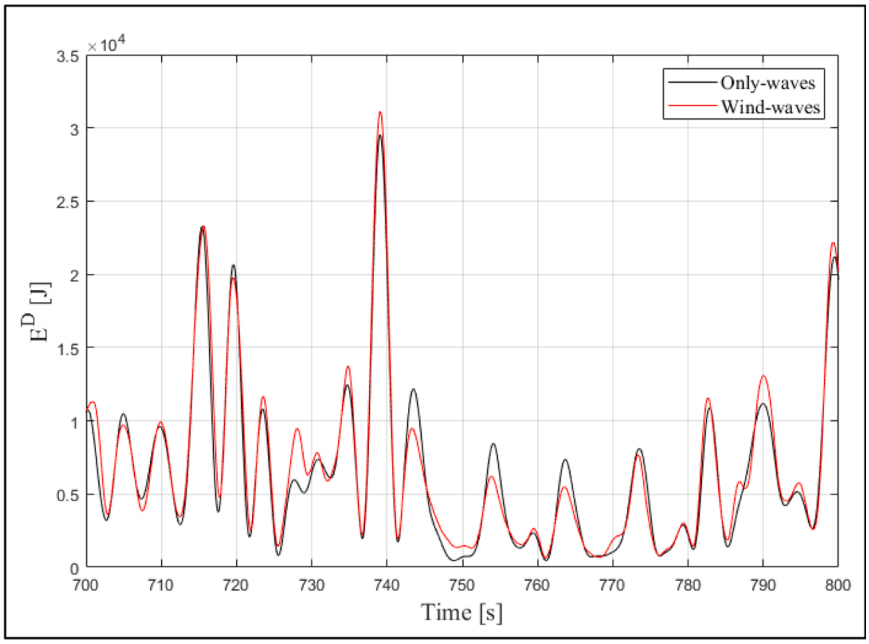

Fig. 19. Dynamic FEM elastic energy comparison between loadcases.

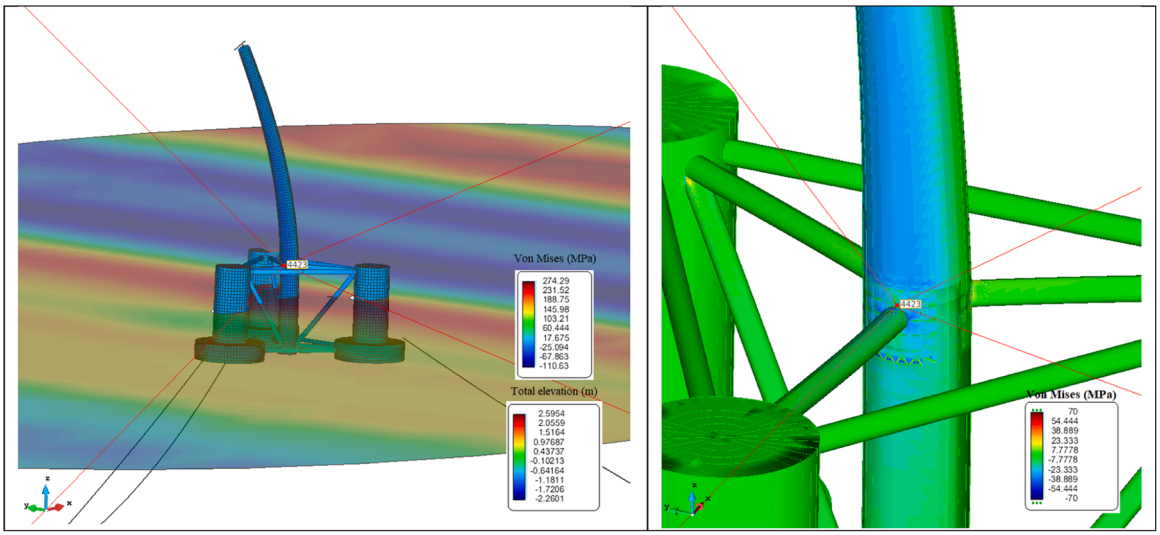

Fig. 20. Left: stress field and deformation in critical condition (def x150). Right: close-up view of the stress field.

Table 12
Energy distribution and cumulative energies from the most energetic modes.

Mode	Modal E^D [J]	E^D [%]	Accumulated E^D [%]
2	5215.50	63.93%	63.93%
11	450.29	5.52%	69.45%
13	379.73	4.65%	74.10%
1	293.47	3.60%	77.70%
17	160.79	1.97%	79.67%

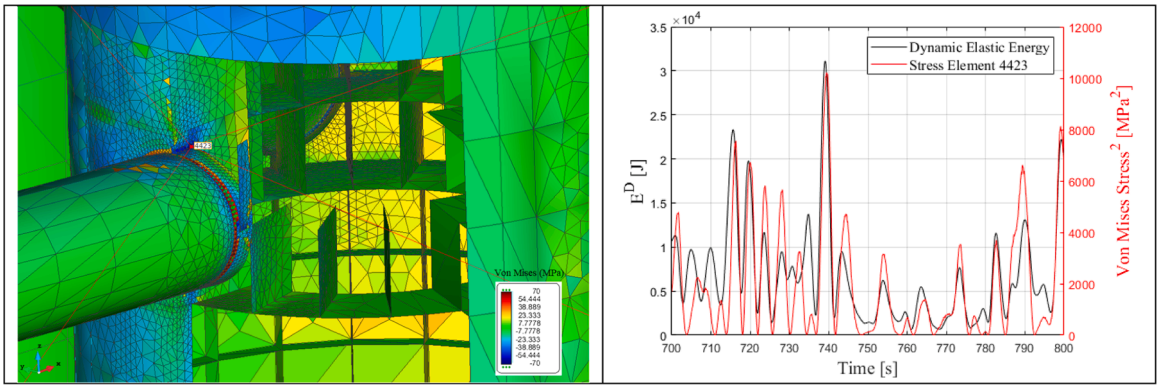

Fig. 21. Stress filed and location of maximum stress hotspot (left). Instantaneous Von Mises stresses at hotspot element and structural energy (right).

The use of a whole time-domain FEM framework, allows a more efficient strong (two-ways) hydroelastic coupling, avoiding the communication among different software, and the importance of using the strong coupling has been analyzed. On the one hand, when considering wet from dry conditions, a significant change in the modal frequency is observed for the lower modes. The weak and strong couplings have been compared versus the conventional quasistatic approach, and the limitations of the quasistatic solution have been tested, underpredicting the dynamic structural response and being unable to capture resonance effects. Hence the capabilities of computing the strong coupling enables to recover the hydroelastic dynamic response in near resonance conditions.

In combination with the wind turbine solver, the proposed work results in a simulation tool for the coupled aero-hydro-elastic response of FOWTs. And this ILA framework allows to execute detailed structural analysis including the elastic behavior of the substructure for the coupled aero-hydrodynamic responses.

Modal response amplitude operators (MRAOs) have been obtained under head waves loading. As the second elastic mode is the most energetic mode under this condition, it has been used for an energy analysis to compare the quasistatic, weak and strong couplings. Large resonance effects are detected, inducing large differences for a wave frequency near modal resonance, and the quasistatic approach fails as expected. Moreover, differences between the weak and strong coupling are also significant due to the change in the modal frequency from dry to wet conditions.

It has been shown also that the modal energy under different irregular waves can be estimated from MRAOs. This information is useful to estimate, a priori, the conditions where structural energy will be higher, to identify most energetic modes (allowing for further reduction of the modal basis), and to check the suitability of the quasistatic, weak and strong couplings.

Funding

This research was funded by the European Commission under the grant agreements H2020 FibreGy (ref. 952,966) and H2020 Fibre4Yards (ref. 101,006,860), and by the Spanish “Ministerio de Ciencia e Innovacion” under the grant agreement MLAMAR (ref. PID2021–126561OB-C31).

CRediT authorship contribution statement

Borja Servan-Camas: Writing – original draft, Supervision, Software, Methodology, Formal analysis, Conceptualization. **Irene Berdugo-Parada:** Writing – original draft, Software, Investigation, Formal analysis. **Julio Garcia-Espinosa:** Writing – review & editing, Supervision, Resources, Methodology, Conceptualization. **Andres Pastor-Sanchez:** Software, Investigation, Formal analysis.

Declaration of competing interest

The authors declare the following financial interests/personal relationships which may be considered as potential competing interests:

Borja Servan Camas reports financial support was provided by European Commission. Borja Servan Camas reports financial support was provided by Spanish Ministry of Science and Innovation. If there are other authors, they declare that they have no known competing financial interests or personal relationships that could have appeared to influence the work reported in this paper.

Appendix

The structural details of the CIMNE-DeepCwind are presented below by components. This structural model will be distributed if requested.

Overall structure:

Fig. 22

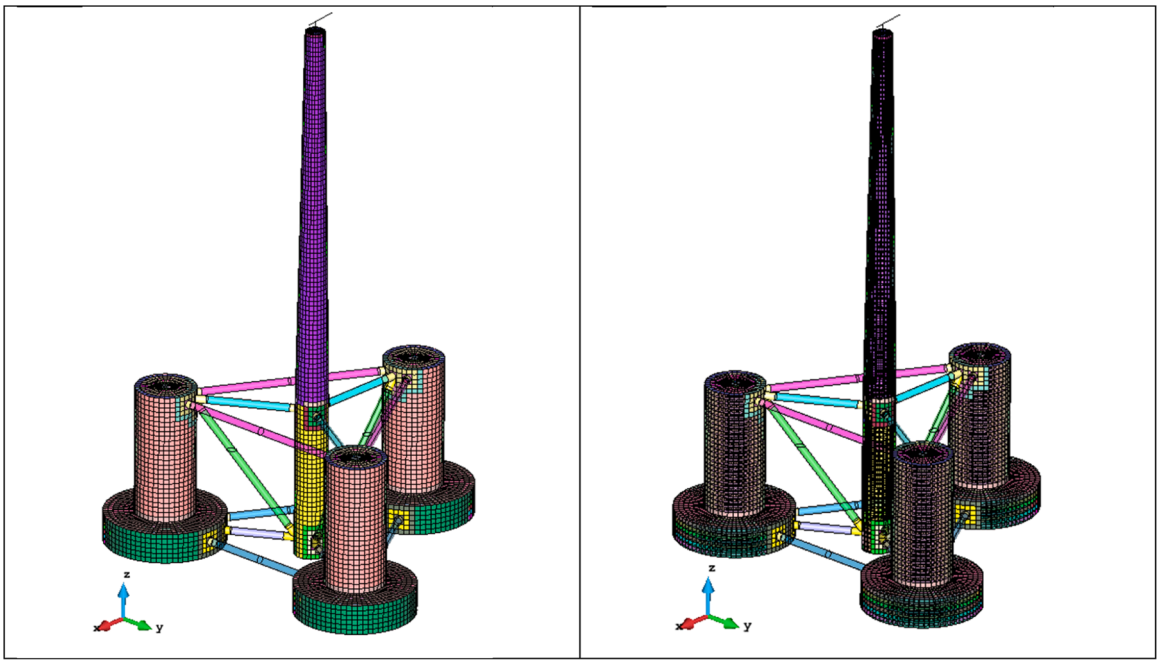

Fig. 22. Left: external structural model. Right: inner reinforcements.

Wind turbine: the wind turbine components are included in the model with punctual masses located at their respective center of mass, see Fig. 23.

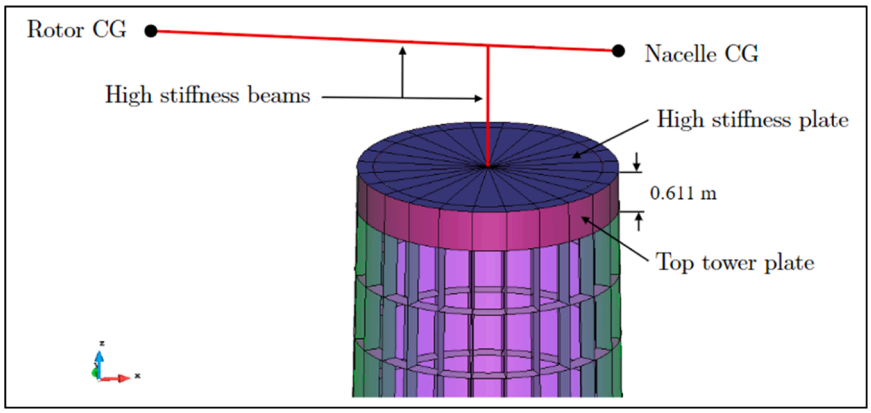

Fig. 23. Wind turbine beam structural model.

The point masses are connected to the top of the tower in the model using high-stiffness, low-density beams. The beam properties are provided in Table 13.

Table 13
Turbine beams particulars.

	Beam Steel Data
Width y, z [mm]	1000, 1000
Young modulus [GPa]	210
Torsion modulus [GPa]	81
Density [kg/m^3]	10.2

Additionally, a high-stiffness plate with considerable thickness is used to transfer the turbine loads to the top of the tower. The top tower plate has different properties from the rest of the tower to ensure a smoother load transfer. The steel particulars are presented in Table 14.

Table 14
Turbine load transfer components.

	Turbine Steel Plate	Top Tower Steel plate
Thickness [mm]	1000	19
Young modulus [GPa]	2100	210
Poisson coefficient [-]	0.3	0.3
Density [kg/m^3]	0.102	8500

Bracing: details of the bracing-columns intersections and close-up views. Additional reinforcement is given to the intersections between braces and columns.
Fig. 24

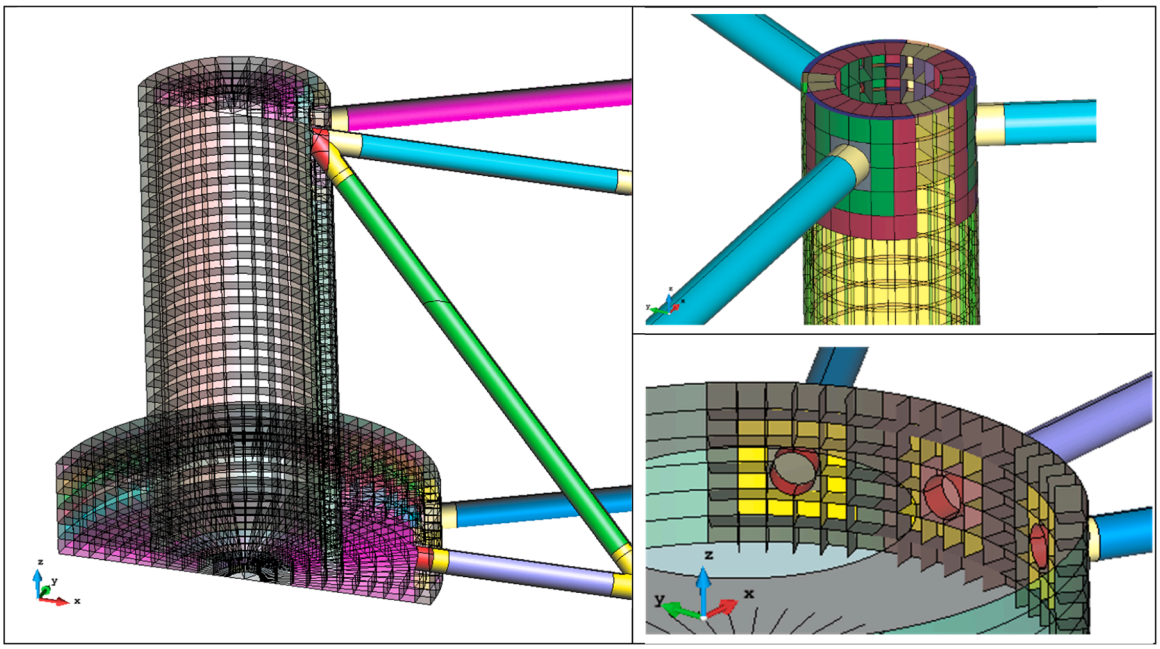

Fig. 24. Intersections between braces and columns.

The bracing steel properties are provided in Table 15.

Table 15
Braces steel properties.

	Braces Plates
Thickness [mm]	17.5
Young modulus [GPa]	210
Poisson coefficient [-]	0.3
Density [kg/m^3]	7845

Central column: cross-section view, measures and stiffeners particulars. Additional reinforcement is given to the area near the tower base.
Fig. 25

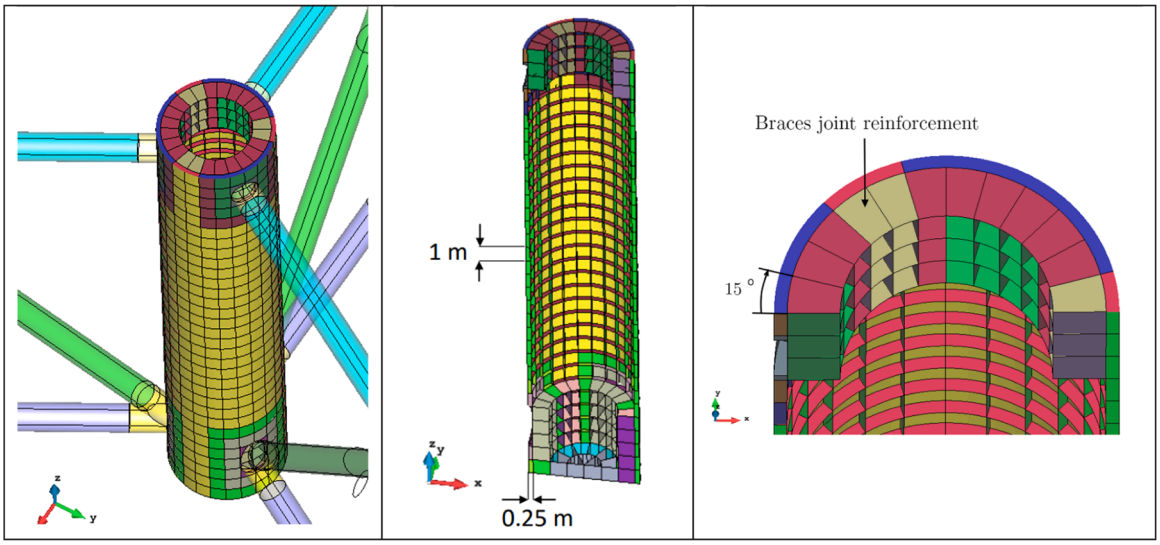

Fig. 25. Left: intersection with braces. Middle: cross-section. Right: top close-up view.

The central column steel properties are provided in Table 16, while the stiffeners distribution is detailed in Table 17. The outer columns share the same steel properties.

Table 16
Central column steel properties.

	Central Column Plates
Thickness [mm]	20
Young modulus [GPa]	210
Poisson coefficient [-]	0.3
Density [kg/m^3]	7845

Table 17
Main column stiffeners particulars.

Central Column Stiffeners Data	
Number of rings [-]	31
Number of longitudinals [-]	24
Number of radials [-]	24
Separation between rings [m]	1
Radial separation between longitudinals [°]	15
Stiffeners width [m]	0.25
Braces joint stiffeners width [m]	1

Outer columns: cross-section view, measures and stiffeners particulars. The column begins at the double bottom of the heave plate. Fig. 26

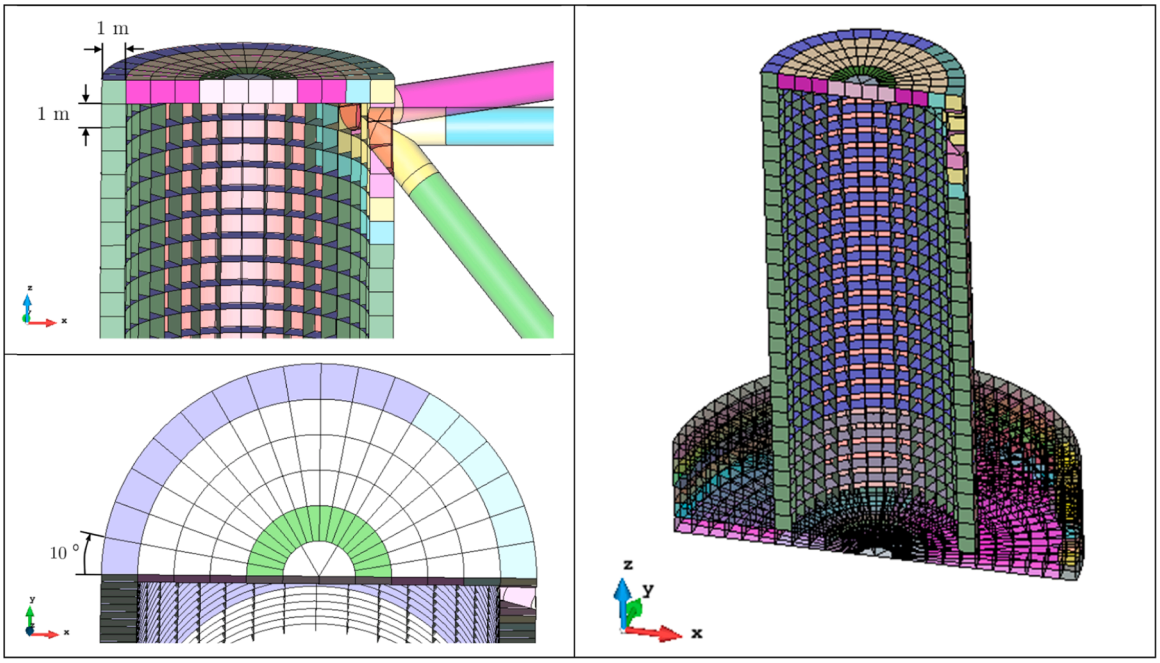

Fig. 26. Left: column details and measures. Right: column cross-section.

The steel properties are given in Table 18, and the stiffener distribution in Table 19.

Table 18
Outer columns steel properties.

	Outer Columns Plates
Thickness [mm]	20
Young modulus [GPa]	210
Poisson coefficient [-]	0.3
Density [kg/m^3]	7845

Table 19
Column stiffeners particulars.

Columns Stiffeners Data	
Number of rings [-]	30
Number of longitudinals [-]	36
Number of radials [-]	36
Separation between rings [m]	1
Radial separation between longitudinals [°]	10
Stiffeners width [m]	1

Heave plates: cross-section view, measures and stiffeners particulars.
Fig. 27

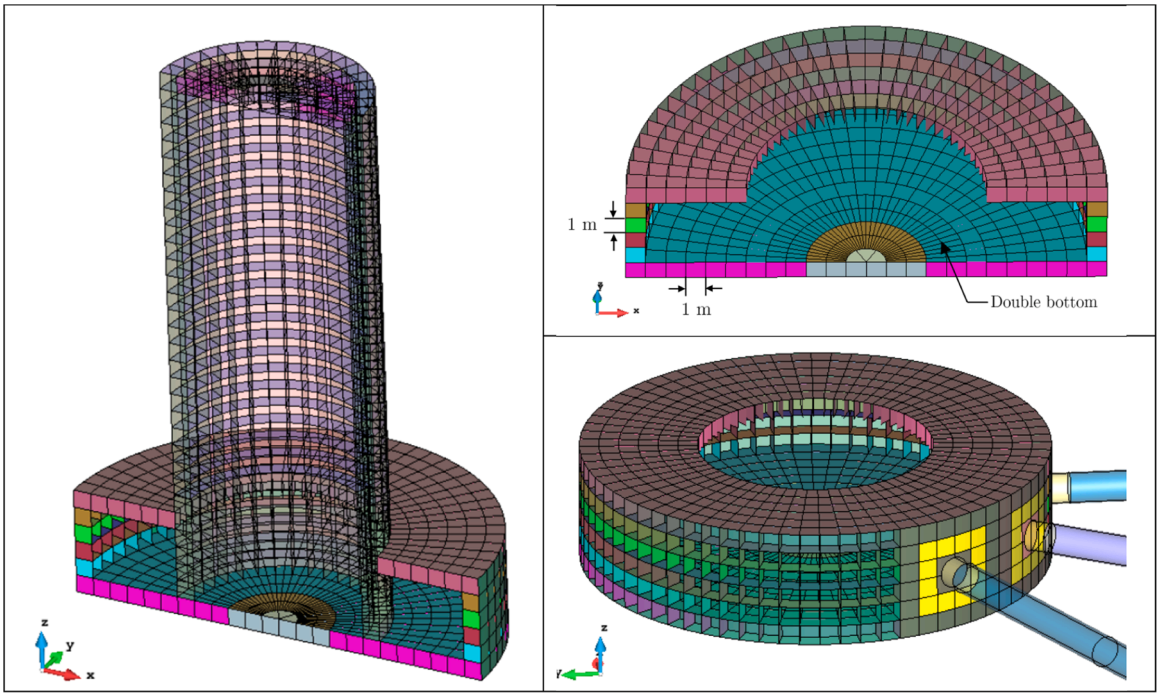

Fig. 27. Left: intersection heave plate-column. Right: Visibility of the heave plate stiffeners.

The heave plate steel properties are provided in Table 20, while the stiffeners distribution is detailed in Table 21.

Table 20
Heave plates steel properties.

	Heave Plates Data
Thickness [mm]	30
Young modulus [GPa]	210
Poisson coefficient [-]	0.3
Density [kg/m^3]	7845

Table 21
Heave plate stiffeners particulars.

Heave Plate Stiffeners Data	
Number of rings [-]	11
Number of longitudinals [-]	72
Number of radials [-]	72
Separation between rings [m]	1
Radial separation between longitudinals [°]	5
Stiffeners width [m]	1

Tower: cross-section view and stiffeners particulars.
Fig. 28

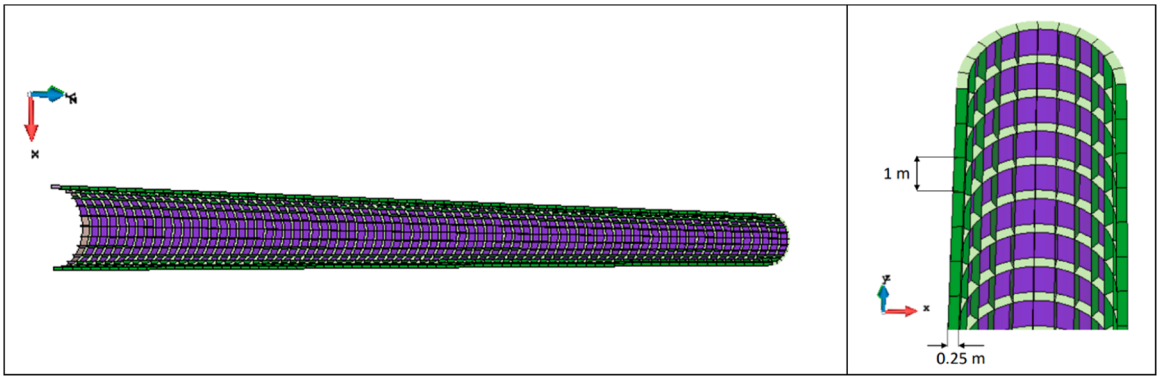

Fig. 28. Left: tower cross-section view. Right: tower-top close-up view.

The tower steel properties are provided in Table 22, while the stiffeners distribution is detailed in Table 23.

Table 22
Tower steel properties.

	Tower Plates
Thickness [mm]	14
Young modulus [GPa]	210
Poisson coefficient [-]	0.3
Density [kg/m^3]	8500

Table 23
Tower stiffeners particulars.

Tower Stiffeners Data	
Number of rings [-]	77
Number of longitudinals [-]	24
Separation between rings [m]	1
Radial separation between longitudinals [°]	15
Stiffeners width [m]	0.25

Data availability

Data will be made available on request.

References

[1] Ran X, Leroy V, Bachynski-Polić E. Hydroelastic response of a flexible spar floating wind turbine: numerical modelling and validation. J Ocean Eng 2023;286 (Part 2):115635. https://doi.org/10.1016/j.oceaneng.2023.115635 [View Article] [Google Scholar].
[2] LIFES50+ Project: qualification of innovative floating substructures for 10MW wind turbines and water depths greater than 50m Deliverable 7.11 design practice for 10MW+ FOWT support structures.
[3] Robertson A. OC7 Project Work Plan, 2024-2027. Implementing agreement for co-operation in the research and development of wind energy systems (IEA wind). Golden, Colorado (USA): National Renewable Energy Laboratory; April 2024.
[4] Jonkman, J.; L. Buhl Jr., M. FAST User's Guide. Technical report NREL/EL-500-38230 August 2005. [View PDF].
[5] Marten, D.; Saverin, J.; Behrens de Luna, R.; Perez-Becker, S. QBlade documentation. Release 2.0.4. 2022. Doi: 10.13140/RG.2.2.19363.12326/2 [View PDF].
[6] Orcaflex documentation. Available online: https://www.orcina.com/webhelp/OrcaFlex/Default.htm (Accessed on 5 July 2024).
[7] Digital Solutions at DNV. Sesam feature description. 2022. [View PDF].
[8] Song H, Damiani R, Robertson A, Jonkman J. A new structural-dynamics module for offshore multimember substructures within the Wind turbine computer-aided engineering tool FAST. In: Conference Paper NREL/CP-5000-5809; 2013 [View PDF] [Google Scholar].
[9] Jonkman J, Damiani R, Branlard Emmanuel, Hall M, Robertson A, Hayman Greg. Substructure flexibility and member-level load capabilities for floating offshore wind turbines in OpenFAST. In: Proceedings of the ASME; 2019. https://doi.org/10.1115/IOWTC2019-7566 [View Article] [Google Scholar].
[10] Servan-Camas S, Di-Capua D, Garcia-Espinosa J, Sa-Lopez D. Fully 3D ship hydroelasticity: monolithic versus partitioned strategies for tight coupling. J Mar Struct Vol 2021;80:103098. https://doi.org/10.1016/j.marstruc.2021.103098 [Google Scholar].
[11] Cao Q, Xiao L, Cheng Z, Liu M. Dynamic responses of a 10 MW semi-submersible wind turbine at an intermediate water depth: A comprehensive numerical and experimental comparison. J Ocean Eng 2021;232:109138. https://doi.org/10.1016/j.oceaneng.2021.109138 [View Article] [Google Scholar].
[12] Li H, Hu Z, Wang J, Meng X. Short-term fatigue analysis for tower base of a spar-type wind turbine under stochastic wind-wave loads. Int J Nav Archit Volume 2018;10(1). https://doi.org/10.1016/j.ijnaoe.2017.05.003 [View Article] [Google Scholar].
[13] Steinacker H, Lemmer F, Raach S, Schlipf D, Wen Cheng P. Efficient multibody modelling of offshore wind turbines with flexible substructures. J Phys Conf Ser 2022. https://doi.org/10.1088/1742-6596/2265/4/042007 [View Article] [Google Scholar].

[14] Bjerg Thomsen J, Bergua R, Jonkman J, Robertson A, Mendoza N, Brown C, Galinos C, Stiesdal H. Modeling the TetraSpar floating offshore wind turbine foundation as a flexible structure in OrcaFlex and OpenFAST. Energies J 2021;14(23):7866. https://doi.org/10.3390/en14237866 [View Article] [Google Scholar].
[15] Li H, Gao Z, Bachynski-Polić E, Zhao Y, Fiskvik S. Effect of floater flexibility on global dynamic responses of a 15-MW semi-submersible floating wind turbine. J Ocean Eng 2023;286(Part 2). https://doi.org/10.1016/j.oceaneng.2023.115584 [View Article] [Google Scholar].
[16] Kwangtae H, Jun-Bae K, Youngjae Y. Hyoung-Seock, S. Structural modeling and failure assessment of spar-type substructure for 5 MW floating offshore wind turbine under extreme conditions in the East Sea. Energy J 2021;14(20):6571. https://doi.org/10.3390/en14206571 [View Article] [Google Scholar].
[17] Park S, Choung J. Structural design of the substructure of a 10 MW floating offshore wind turbine system using dominant load parameters. J Mar Sci Eng 2023; 11(5):1048. https://doi.org/10.3390/jmse11051048 [View Article] [Google Scholar].
[18] Garcia-Espinosa J, Servan-Camas B, Calpe-Linares M. High fidelity hydroelastic analysis using modal matrix reduction. J Mar Sci Eng 2023;11:1168. https://doi.org/10.3390/jmse11061168 [Google Scholar].
[19] Servan-Camas B, García-Espinosa J. Accelerated 3D multi-body seakeeping simulations using unstructured finite elements. J Comput Phys 2013;252:382–403. https://doi.org/10.1016/j.jcp.2013.06.023 [Google Scholar].
[20] Servan-Camas B. A time-domain finite element method for seakeeping and wave resistance problems- doctoral thesis. School of Naval Architects and Marine Engineers. Technical University of Madrid; 2016 [Google Scholar] [View PDF].
[21] Garcia-Espinosa J, Di Capua D, Servan-Camasa B, Ubach P-A, Oñate E. A FEM fluid–structure interaction algorithm for analysis of the seal dynamics of a surface-effect ship. J Comput Methods Appl Mech Engrg 2015;295:290–304. https://doi.org/10.1016/j.cma.2015.07.010 [Google Scholar].
[22] Gutierrez-Romero JE, García-Espinosa J, Servan-Camas B, Zamora-Parra B. Non-linear dynamic analysis of the response of moored floating structures. J Mar Struct 2016;49:116e137. https://doi.org/10.1016/j.marstruc.2016.05.002 [Google Scholar].
[23] Serván-Camas B, Cercós-Pita JL, Colom-Cobb J, García-Espinosa J, Souto-Iglesias A. Time domain simulation of coupled sloshing–seakeeping problems by SPH–FEM coupling. J Ocean Eng 2016;123:383–96. https://doi.org/10.1016/j.oceaneng.2016.07.003 [Google Scholar].
[24] Servan-Camas B, Gutierrez-Romero JE, García-Espinosa J. A time-domain second-order FEM model for the wave diffraction-radiation problem. Validation with a semisubmersible platform. Mar Struct 2018;58:278–300. https://doi.org/10.1016/j.marstruc.2017.12.001 [Google Scholar].
[25] Garcia-Espinosa, J; Servan-Camas, B. A non-linear finite element method on unstructured meshes for added resistance in waves. J Ships Offshore Struct DOI: 10.1080/17445302.2018.1483624 [Google Scholar].
[26] Jonkman J, Sclavounos P. Development of fully coupled aeroelastic and hydrodynamic models for offshore wind turbines. In: Proceedings of the ASME Wind Energy Symposium Reno, Reno, NV, USA; 2006. p. 9–12 [View PDF] [Google Scholar].
[27] Jonkman, JM. Dynamics modeling and loads analysis of an offshore floating wind turbine. Technical Report NREL/TP-500-41958. 2007. [View PDF] [Google Scholar].
[28] Pacheco-Blazquez R, Garcia-Espinosa J, Di Capua D. Pastor Sanchez, A. A digital twin for assessing the remaining useful life of offshore wind turbine structures. J Mar Sci Eng 2024;12(4):573. https://doi.org/10.3390/jmse12040573 [Google Scholar].
[29] OSI4IOT Platform. Available online: https://github.com/osi4iot/osi4iot (accessed on 24 March 2024).
[30] Di Capua, D.; Pacheco, R.; García-Espinosa, J.; Pastor, A. OSI4IOT: An advanced open-source platform for sensor-driven IoT and digital twins deployment. Available online: https://www.researchgate.net/publication/372883021_OSI4IOT_An_Advanced_Open-Source_Platform_for_Sensor-driven_IoT_and_Digital_Twins_Deployment (accessed on 24 March 2024).
[31] https://www.compassis.com/compass/es/Productos/SeaFEM.
[32] https://www.compassis.com/compass/es/Productos/RamSeries.
[33] Felippa C, Haugen B. A unified formulation of small-strain corotational finite elements: I. Theory. Comput Methods Appl Mech Eng 2005;194:2285–335.
[34] Felippa CA. A study of optimal membrane triangles with drilling freedoms. Comput Methods Appl Mech Eng 2003;192:2125–68.
[35] Dhatt G. An efficient triangular shell element. AIAAJ 1970;8:2100–2.
[36] Almeida FS, Awruch AM. Corotational nonlinear dynamic analysis of laminated composite shells. Finite Elements in Anal Des 2011;47:1131–45.
[37] Patalano S, Mango Furnari A, Vitolo F, et al. A critical exposition of model order reduction techniques: application to a slewing flexible beam. Arch Comput Methods Eng 2019. https://doi.org/10.1007/s11831-019-09369-1 [Google Scholar] [View Article].
[38] Irons BM, Tuck RC. A version of the Aitken accelerator for computer iteration. Int J Numer Methods Eng 1969;1:275–7.
[39] Berdugo-Parada I, Servan-Camas B, Garcia-Espinosa J. Numerical framework for the coupled analysis of floating offshore multi-wind turbines. J Mar Sci Eng 2024;12:85. https://doi.org/10.3390/jmse12010085 [Google Scholar].
[40] Robertson, A.; Jonkman, J.; Masciola, M.; Song, H.; Goupee, A.; Coulling, A.; Luan, C. Definition of the semisubmersible Floating system for phase II of OC4. Technical Report NREL/TP-5000-60601. 2014. Doi: 10.2172/1155123 [View PDF] [Google Scholar].
[41] Jonkman, JM.; Butterfield S.; Musial, W.; Scott, G. Definition of a 5-MW reference wind turbine for offshore system development. Technical Report NREL/TP-500-38060. 2009. Doi: 10.2172/947422 [View PDF] [Google Scholar].
[42] Robertson A, Jonkman J, Vorphal F, Popko W, Qvist J, Frøyd L, Chen X, Azcona J, Uzunoglu E, Guedes Soares C, Luan C, Yutong H, et al. Offshore code comparison collaboration continuation within IEA wind task 30: phase II results regarding a floating semisubmersible wind system. In: 33rd International Conference on Ocean, Offshore and Arctic Engineering; 2014. https://doi.org/10.1115/OMAE2014-24040 [View PDF] [Google Scholar].
[43] Robertson A, Jonkman J, Masciola M, Molta P, Goupee A, Coulling A, Prowell I, Browning J. Summary of conclusions and recommendations drawn from the DeepCWind scaled floating offshore wind system test campaign. In: ASME 2013 32nd International Conference on Ocean, Offshore and Arctic Engineering; 2013. https://doi.org/10.1115/OMAE2013-10817 [View PDF] [Google Scholar].
[44] Bureau Veritas. Classification and certification of floating offshore wind turbines. 2019 Rule Note NI 572 DT R02 E. [View PDF].
[45] IEC International Electrotechnical comission standard on wind turbines. Part 1: Des Requ 2005:61400–1.
[46] Vigara F, Cerdán L, Durán R, Muñoz S, Lynch M, Doole S, Molins C, Trubat P, Guanche R. D1.2 Design basis. Corewind 2019 [View PDF].